Journal of Structural Geology 187 (2024) 105213

Contents lists available at ScienceDirect

Journal of Structural Geology

journal homepage: www.elsevier.com/locate/jsg

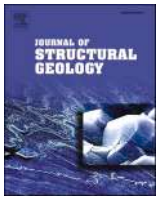

Enhanced structural analysis through a hybrid analogue-digital mapping approach: Integrating field and UAV survey with microtomography to characterize metamorphic rocks

E. Fazio [a,*], G. Ortolano [a], G.I. Alsop [b], A. D'Agostino [a], R. Visalli [a], V. Luzin [c], F. Salvemini [c], R. Cirrincione [a]

[a] Università di Catania - Dpt. Sc. Biol. Geol. Amb., Corso Italia 57, 95129, Catania, Italy
[b] School of Geosciences, University of Aberdeen, Aberdeen, AB24 3UE, United Kingdom
[c] ANSTO Sydney, Australia

ARTICLE INFO

Keywords:
Shear zone
Mylonites
Kinematics
Sheath folds
UAV-Survey
3D VOM (virtual outcrop model)

ABSTRACT

This study focused on collecting structural data orientations of a crustal-scale shear zone (Palmi Shear Zone, PSZ, southern Calabria, Italy) by integrating various analytical and field-based techniques. The PSZ consists of deformed metamorphic rocks (migmatitic biotitic paragneiss, marbles, and skarns) showing multiple folding phases, and Hercynian tonalites and pegmatites (306-290 Ma), crosscut by Late Hercynian leucocratic dykes (ca. 290 Ma). Multi-sized clasts composed of different lithologies are preserved on clean outcrop surfaces, and are sheared into both σ - and δ -type objects that collectively suggest opposing senses of shear. The study incorporates structural analysis of folds, field and aerial surveys (UAV), digital mapping, and microcomputed tomography. Various kinematic indicators were observed in the PSZ, indicating a mix of factors influencing the shear strain patterns (e.g. fold interference patterns, different rock types with high viscosity contrast). The findings suggest a clear consistency between structural data inferred from 3D VOM (Virtual Outcrop Model) and those collected directly in the field, confirming the occurrence of both sinistral and dextral shear in the PSZ, providing important insights into the tectonic evolution of the Calabrian-Peloritani Terrane.

1. Introduction

It is widely known, through geological records and geophysical surveys, that crustal-scale deformation often occurs in high-strain zones (Platt and Behr, 2011). These zones, known as crustal-scale shear zones (Ramsay, 1980; Fossen and Cavalcante, 2017), typically have a tabular shape with intricate anastomosing networks and a well-developed mylonitic foliation often accompanied by a stretching lineation (Carreras et al., 2005; Alsop and Holdsworth, 2002). These structural features are critical for determining a deformed area's main tectonic transport direction (e.g. Tavarnelli et al., 2004; Xypolias, 2010). The tectonic history of a crystalline complex can be traced by analyzing the geometric relationships between foliations, fold hinges, and lineations (e.g. Alsop et al., 2021; Arslan et al., 2008). In these zones, a variety of fold geometries with kinematic complexity are common, which can complicate the determination of shear sense (Holdsworth et al., 2002; Fazio et al., 2018), leading to potential challenges in determining the sense of shear (Grasemann et al., 2003; Mukherjee, 2017; Fazio, 2019). Within mid-crustal shear zones, folds may rotate and develop curvilinear hinges (i.e. sheath folds; Mies, 1993; Alsop and Holdsworth, 2012; Alsop et al., 2010; Fazio et al., 2024) resulting in a range of obliquities with respect to the tectonic transport direction (oblique folds; Ramsay, 1980; Alsop, 1992; Carreras et al., 2005). When conducting a kinematic investigation, it is essential to consider the impact of local heterogeneities on finite strain as well as the various lithologies and viscosities involved in deformation. These differences in rock type give rise to appreciable rheological contrasts that simultaneously generate extremely intricate structures, that may simulate interference patterns (Ramsay, 1980; Druguet et al., 2009). Progressive refolding of pre-existing folds is commonly preserved in ductile shear zones and may generate typical rolling patterns (Platt, 1983).

Monoclinic (Passchier, 1998) or triclinic symmetry of shear zones (Lin et al., 1998; Iacopini et al., 2010) also provides an important control on the resulting structures. Indeed, the 3D model of partitioned triclinic

* Corresponding author.
E-mail address: eugenio.fazio@unict.it (E. Fazio).

https://doi.org/10.1016/j.jsg.2024.105213
Received 17 October 2023; Received in revised form 1 July 2024; Accepted 8 July 2024
Available online 9 August 2024

transpressional strain by Tavarnelli et al. (2004), shows that dextral-shear in contraction-dominated domains may develop coevally with sinistral-shear zones in wrench-dominated domains. Various models have been proposed to explain the kinematic complexity of shear zones via investigations of fold geometry (e.g. Holdsworth et al., 2002; Carreras and Druguet, 2019; Vitale and Mazzoli, 2008; Xypolias and Alsop, 2014). Shear zones with strike-slip kinematics have additional complexities, such as structural interference patterns related to partitioning between transtensional and transpressional domains (Dewey et al., 1998). Moreover, shear zones may reactivate at a later stage, with opposing transport directions (Holdsworth et al., 2001; Reddy et al., 2003; Piette-Lauzière et al., 2020).

In this study we present structural field data collected from the Palmi crustal-scale shear zone (PSZ) first recognized by Prosser et al. (2003) developed in the Calabria Peloritani Terrane (Cirrincione et al., 2015 and references therein; Fig. 1). This shear zone crops out between the Aspromonte (Ortolano et al., 2005; Fazio et al., 2008) and Serre massifs near the village of Palmi (southern Calabria, Italy; Ortolano et al., 2020). The rocks outcropping on the Palmi coast were originally described by Cortese (1885) and then, in the second half of the 20th century, in a brief geological note by Bertolani and Loschi Ghittoni (1977) on the occurrence of impure marbles.

To decipher the structural evolution of the PSZ, we reconstructed a three-dimensional virtual outcrop via SfM (Structure from Motion), and used aero-photogrammetry techniques from commercial drones to supplement the structural database collected via traditional fieldwork. Moreover, on a selection of mylonitic rock samples we also characterized microstructures and inferred mineral phases volumetric distribution by means of microtomography (Aerden and Ruiz-Fuentes, 2020; 2022). This combined approach, using UAV (Unmanned Aerial Vehicles), was a positive addition to fieldwork, especially where accessibility to exceptional exposures was inhibited due to sub-vertical sea cliffs. The use of UAV to determine the orientation of geological features has been successfully adopted in recent years (e.g. Vasuki et al., 2014; Bond and Cawood, 2021; Smeraglia et al., 2021; Tavani et al., 2022 and references therein).

Our aim is to emphasize the great potential in applying UAV-surveys and 3D-VOM analysis to acquire structural data which help to reconstruct the kinematic evolution of an high strain zone by applying a multisource and multiscale approach.

2. Regional geologic setting

The Calabrian Peloritani Terrane (CPT, Figs. 1 and 2a) represents a strongly arcuate orogenic terrane, mostly composed of Variscan basement relics (e.g. Micheletti et al., 2008), presently incorporated within the Apennine-Maghrebide chain (Cirrincione et al., 2015; Vitale et al., 2019). Its origin is still debated due to the difficult palinspastic location along the border of the southern European Variscan chain (von Raumer et al., 2003, 2013; Schulmann et al., 2022), its later geodynamic behavior during the opening of the Alpine Tethys (van Hinsbergen et al., 2020), and the relatively rapid closure along curvilinear plate or microplate margins.

In this context, we use innovative multiscale and multisource data collected from the PSZ located at the northern edge of the southern Calabrian Peloritani Terrane (Fig. 1b). According to Ortolano et al. (2020), the PSZ is a relic fragment of an anastomosed mylonitic strike-slip system that has driven the formation of the Western Mediterranean area (Fig. 1a). This early Alpine strike-slip deformation was triggered by the Adria indentation against the Euro-Asian block, with a consequent rotation and translation of the Sardinia-Corsica Block. The PSZ, which is roughly 400 m wide and outcrops for 1500 m along strike (Fig. 2a), contains a very well-preserved mylonitic fabric with at least three distinct lithologies that exhibit various rheological behaviours (Prosser et al., 2003; Ortolano et al., 2013, 2020 - Fig. 3a).

From the geological point of view, the PSZ separates sillimanite-bearing paragneisses, which are exposed to the north, from the strongly anisotropic tonalites, which crop out to the south (Grande et al., 2009; Rovaglioso locality, Fig. 2a). These tonalites are the older and deeper plutonic products of the Serre Massif late-Variscan batholith system (Angì et al., 2010; Fiannacca et al., 2017, 2021; Russo et al., 2023) and are characterized by elongated ellipsoidal microgranular mafic enclaves (MMEs) up to 1.5 m in length, suggesting syn-tectonic Late Hercynian magmatism. Their continuity is interrupted by several pegmatitic dykes (ranging from centimeter to pluri-meter thick) as well as by centimeter thick pseudotachylyte injection veins of Alpine age (30 Ma, Grande et al., 2009). Furthermore, they exhibit a strong foliation mainly N198/56 (dip direction/dip) with a strike orientation roughly subparallel to the main mylonitic foliation of the subvertical PSZ.

From the rheological point of view, most of the strain is preferentially partitioned into Ca-silicate bearing rocks (Prosser et al., 2003; Festa et al., 2015; i.e., the skarns of Ortolano et al., 2020), which concentrate most of the deformation with respect to other lithotypes. Low-strain domains of varying sizes, primarily composed of poorly deformed tonalites and subsequently more or less migmatitic paragneisses, are found within the shear zone (Fig. 3 and Supplementary Figs. S1–S7). Locally, mylonitic to ultramylonitic gneisses can also be observed as formed at the expense of aplitic-pegmatitic dykes intruding the foliated tonalites. Previous studies based on vorticity analysis (Festa et al., 2015; Ortolano et al., 2020) suggest that the skarns, marbles, and Ca-silicate bearing rocks exhibit strain localization recording a simple shear component of up to 42% compared to the mylonitic paragneisses and tonalites, which show lower values ranging between 32 and 38% indicating stronger domains. The most intense ductile strain is recorded at the boundary between Hercynian intrusive rocks outcropping southward at the Rovaglioso location (Fig. 2b; strongly foliated amphibole-bearing tonalites), and the hosting migmatitic rocks that occur northward at the beach of Taureana (Fig. 3). Because of this highly contrasting rock rheology, different kinematic interpretations of the PSZ zone have been proposed. For instance, Festa et al. (2020) interpret the kinematics to be consistent with a left-lateral strike-slip deformation associated with transport toward the WNW (i.e., Euro-verging in the current geographic coordinates). Alternatively, Ortolano et al. (2020) suggest that the PSZ represents a relic anastomosed branch of a right-lateral strike-slip shear zone that, since the Eocene, caused the strike-slip movement of the southern Calabrian Peloritani Orogen from Africa to the Mediterranean region by accommodating some strike-slip Eocene-Oligocene geodynamics.

Petro-structural investigations conducted by Prosser et al. (2003) in the same area determined an Alpine age (Rb-Sr mica) between 51 Ma and 56 Ma for rocks involved in the PSZ. This was interpreted as an Early Eocene sinistral shear zone that was active along an E-W direction and southwards along near-vertical lineations.

The pervasive sub-vertical mylonitic foliation (S_M) is characterized by a dominant WNW-ESE trend (Fig. 2a–b). However, despite the continuous exposure which is little altered in outcrop, especially around the Ulivarella stacks (Fig. 2b and 3), the kinematics of the PSZ still remain controversial (Festa et al., 2020; Ortolano et al., 2020). A distinctive feature within these outcrops is the preservation of sheath-folds (e.g. Alsop and Carreras, 2007 for definitions), which form as a result of progressive deformation caused by the presence of more competent blocks of tonalite and paragneissic blocks dispersed within metacarbonate rocks.

3. Materials and methods

3.1. Field measurements and UAV-LiDAR survey

Spatial orientation of structural surfaces (strike/dip) and lineations (plunge/trend) were collected in the field using both a traditional geological compass as well as by digital technology (Clino FieldMove app) (Figs. 3 and 4). Both techniques provided consistent results.

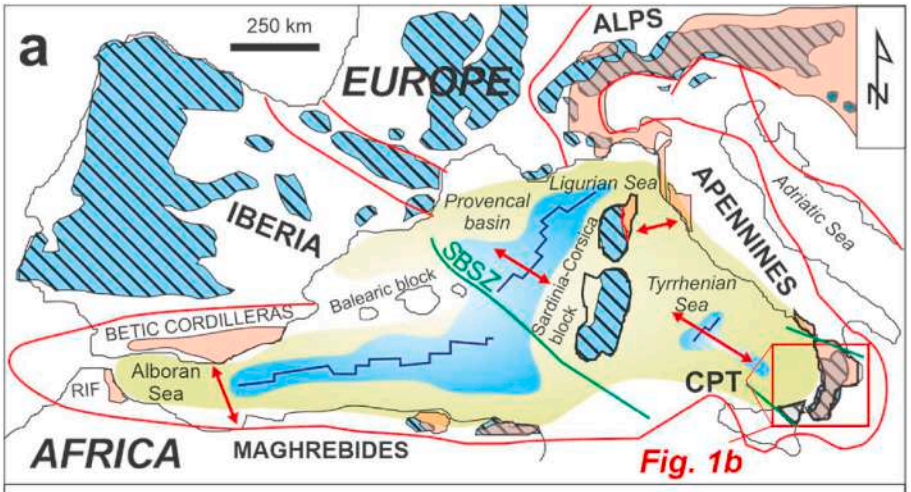

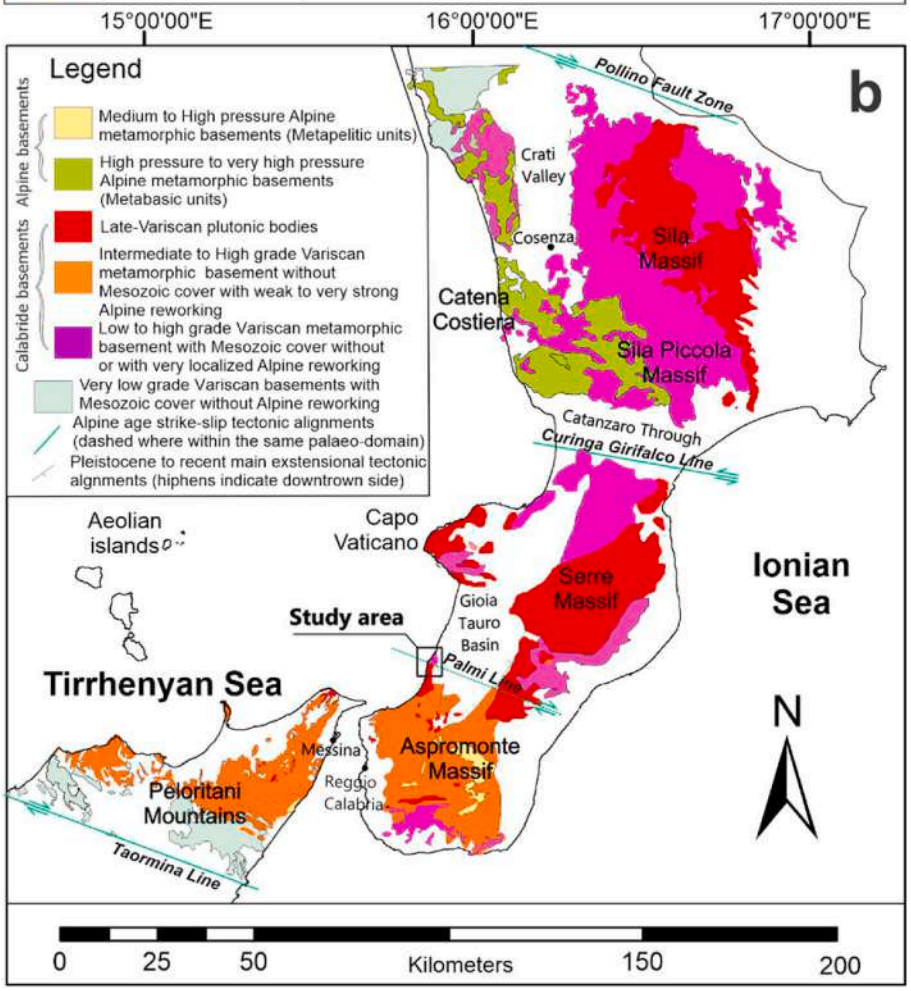

(caption on next page)

Fig. 1. (a) Geological framework of the Western Mediterranean area showing the present-day distribution of the Alpine and Pre-Alpine Basements in the western Mediterranean realm with the study area location (red square area); abbreviations: CPT (Calabrian Peloritani Terrane). (b) Distribution of the basement units in the Calabrian Peloritani Terrane subdivided per type of metamorphism; the study area location is shown. (For interpretation of the references to color in this figure legend, the reader is referred to the Web version of this article.)

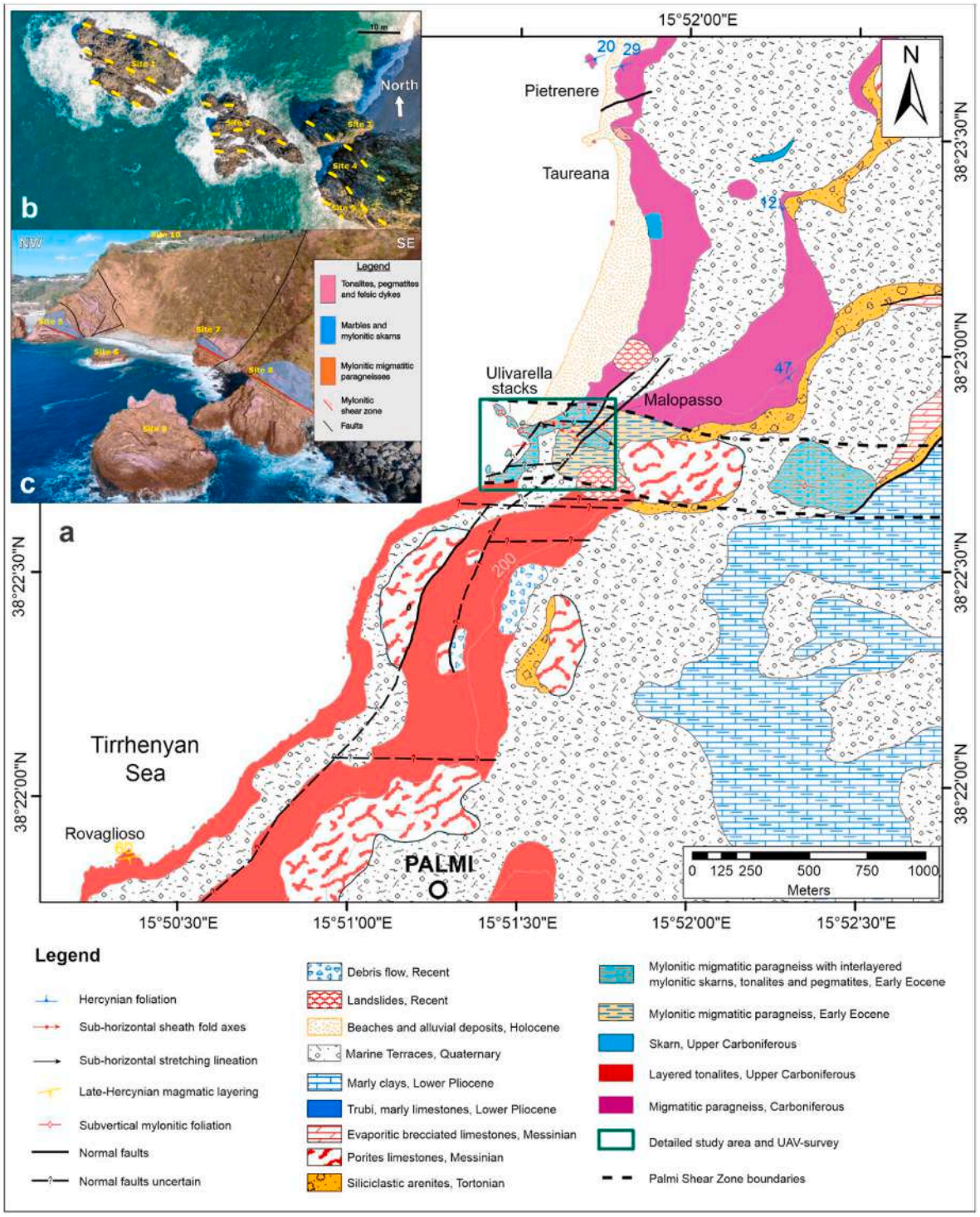

Fig. 2. (a) Geological map of the Palmi Shear Zone (PSZ) area (modified from Ortolano et al., 2020); the green squared area represents the region where aerial survey and digital mapping has been focused. (b) Aerial view of the Ulivarella stack region (UAV survey Sites 1–5) with traces of mylonitic foliation (yellow dashed lines); (c) aerial view of the coastline where PSZ is exposed, showing UAV sites location; main structures (faults and shear zones) are also shown. (For interpretation of the references to color in this figure legend, the reader is referred to the Web version of this article.)

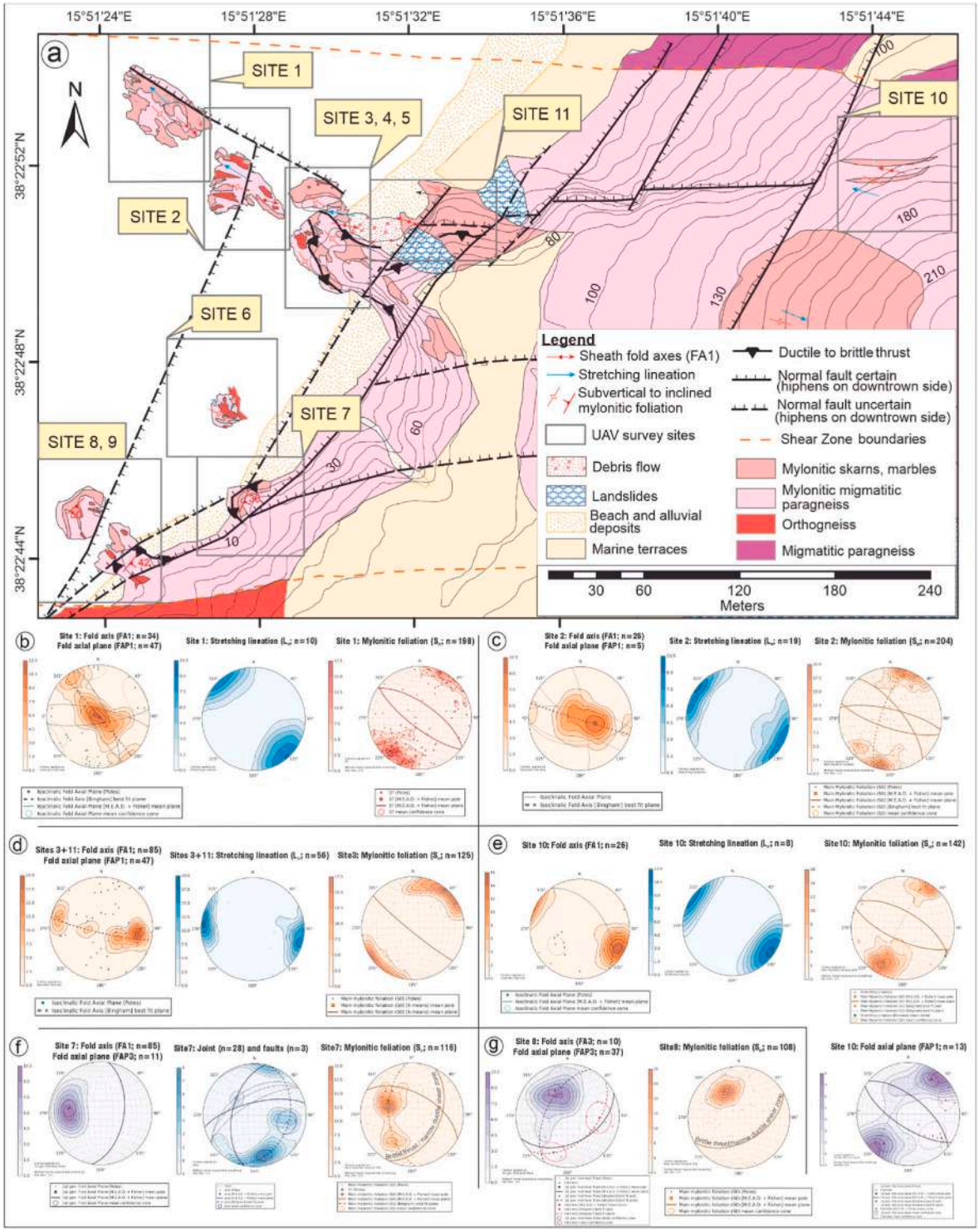

Fig. 3. Structural geological map of the Palmi Shear Zone (see Fig. 2a for location) with stereoplots of the field based structural data and location of the UAV survey sites: (a) Geological map of the Palmi shear zone related mylonites with average values of the structural data; b-g) Stereoplots of the field and aerial based structural features, fold axes and fold axial planes of the sheath folds, mylonitic foliation, and of the stretching lineations related to the mylonitic fabric for the sites 1, 2, 3, 7, 8, 10, and 11. The UAV surveys structural features are available on the supplementary materials for each sites with high resolution structural maps per each site.

We performed several UAV missions to gain aerial views of outcrops from different perspectives, with the maximum elevation of the camera being 10 m above the terrain. In particular, we selected clean exposures where folding is recognizable on photographs taken by a UAV at a minimum distance of 5 m from the outcrop on subvertical slopes. The main purpose of such drone surveys is to infer the orientation of structures (e.g. fold axial surfaces, foliations, fold hinge lines) from digitally reconstructed 3D virtual outcrop models. This allows us to enhance the manually collected data with this additional information. We therefore extended virtual analyses into outcrops where no field data have been collected. This approach is quick, enables safe interpretation on very steep outcrop faces, and is cost-effective. The workflow followed in this study is shown in Fig. 4. Field measurements of foliation orientations were used for calibration of the virtual models, enabling construction of

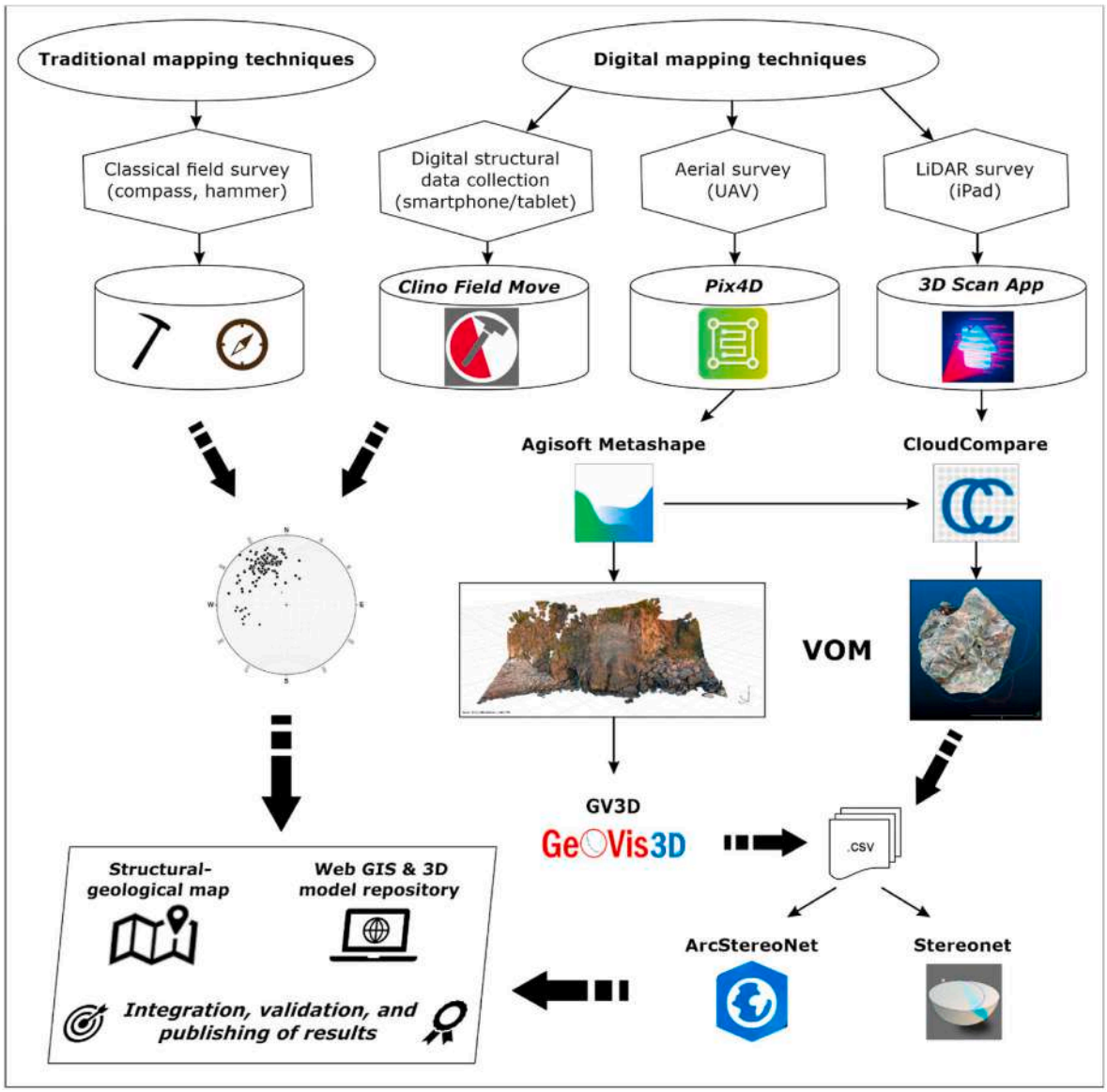

Fig. 4. Workflow chart showing the various steps of this study and processes of data gathering via traditional and digital mapping techniques.

a statistically robust dataset of planar structures inferred by the virtual outcrop model (VOM).

For the aerial survey, a UAV type DJI multi-copter was used; Model aircraft: Mavic 2 Pro (four propellers) equipped with both automatic and manual radio controllers (models RM500 and RC1A). For this study that aims to infer the spatial orientation of geological structures, we used an aircraft with onboard GPS. There was therefore no need for a cm-precision GPS device like a total station (see Cawood et al., 2017 and references therein regarding a comparison of SfM techniques and relative results).

On some occasions (e.g., site 11, see Fig. 3 and Table 1 for location and details) a LiDAR (Light Detection and Ranging) survey was also undertaken to capture details of smaller volumes of outcrop. The site of interest was walked over with a LiDAR sensor mounted on an iPad (Pro

Table 1
Study sites selected for 3D-virtual outcrops.

Site N.	Station name	Field-survey	UAV-survey	Latitude	Longitude	Altitude outcrop range (mt a.s.l.)
1	*Reef 1 - Ulivarella*	*Y*	*Y*	38°22′52.94″N	15°51′26.05″E	*0–18*
2	*Reef 2 - flat stack*	*Y*	*Y*	38°22′51.68″N	15°51′27.58″E	*0–4*
3	*Tower*	*Y*	*Y*	38°22′51.18″N	15°51′29.96″E	*0–18*
4	*Black cliff*	*Y*	*Y*	38°22′50.49″N	15°51′29.57″E	*0–15*
5	*Stairs cliff*	*N*	*Y*	38°22′50.01″N	15°51′29.17″E	*0–20*
6	*Trakini sea-stack*	*N*	*Y*	38°22′47.06″N	15°51′27.06″E	*0–3*
7	*Trakini fold*	*N*	*Y*	38°22′45.38″N	15°51′27.37″E	*0–9*
8	*Sigmoid-megaclast*	*N*	*Y*	38°22′44.22″N	15°51′24.80″E	*0–12*
9	*Fold interferences sea-stack*	*N*	*Y*	38°22′44.88″N	15°51′23.40″E	*0–11*
10	*Malopasso*	*Y*	*Y*	38°22′51.83″N	15°51′44.41″E	*132–148*
11	*Tauerana beach cliff*	*Y*	*Y*	38°22′51.48″N	15°51′32.34″E	*0–30*

11″ model). This allows rapid acquisition and elaboration of 3D (a few m^3) volumes of interest (see Tavani et al., 2022 for a detailed study of this technique).

We adopted 'PiX4D capture' (free license) for planning flying-missions, and 'Agisoft Metashape Professional' (v.1.8.4, academic license) for processing aerial images, point cloud reconstructions, and 3D models by means of SfM (Structure from Motion) techniques. We then exported: 1) KMZ tiled models that were analyzed by 'GeoVis3D' (free license) and, 2) point clouds of outcrops to be analyzed by 'CloudCompare' software with the Compass plugin (Thiele et al., 2017). Orientations inferred by the 3D virtual outcrop models (VOM) were plotted by using 'ArcStereoNet' (Ortolano et al., 2021) and 'Stereonet' (Cardozo and Allmendinger, 2013).

For LiDAR acquisitions, we used two different applications installed on iPad available in the Apple store (https://apps.apple.com/): '3D Scanner App' (Laan Labs) and 'Scaniverse - 3D scanner' (Toolbox AI).

ArcGIS Pro was also used to realize structural maps of the study area by comparing data inferred from 3D VOM and those collected directly in the field by geological compass or with Clino App (Fig. 3 and Supplementary Figs. S1–S7). GeoVis3D (https://www.ausgeol.org/geovis3d/) incorporates tools for the measurement of planar and linear elements of 3D geological models, and also provides tools for 3D annotation and labelling. GeoVis3D accepts 3D models as KMZ files that were created using the Agisoft photogrammetry software.

3.2. Fabric analysis and microcomputed tomography

A quartz-rich calc-silicate bearing rock specimen (PAL-EF; Fig. 5) collected at station 11 (Taureana beach) was analyzed by acquiring SEM-EDS X-ray elemental maps from a thin section of the same sample and then processed to identify the modal amounts of the mineral phases. An automatic mineral classification (Fig. 5c) was performed with the software X-Min Learn (D'Agostino, 2023), employing a machine learning model previously trained with other samples collected near PAL-EF. The model achieved a decent classification that was only slightly refined using the tools provided by the software itself. Such a classification was further integrated and verified through micro-tomography investigation of the same specimen revealing the volumetric distribution of phases as well.

This investigation was carried out at the ANSTO laboratory in Sidney, Australia, where the CPO (crystallographic preferred orientation) of the main constituting minerals was measured by means of neutron diffraction (Fig. 6).

The beamline was configured in high-resolution configuration, corresponding to a L/D ratio of 1000 (where L is the distance between the beam collimator to the image plane, and D the diameter of the collimator). The neutron imaging data were acquired via a Photometrics 5 Megapixel (5056 x 2968) IRIS CMOS sensor camera coupled with a 100 mm lens to yield images with a pixel size of 14.7 μm. The detector system was equipped with a 30 μm thick Gd2O2S:Tb scintillation screen. A total of 3 accumulations with an exposure of 19s were acquired at each angular step with an increment of 0.1° over 360°. Flat field normalization with dose correction, dark current subtraction, ring artefacts suppression in frequency and real space domains were applied to the raw data. The neutron tomography stacks were computed using the Octopus Reconstruction software (Dierick et al., 2004). The Avizo 2023.1.1 software was employed for data visualization and evaluation (https://www.thermofisher.com/au/en/home/electron-microscopy/pro

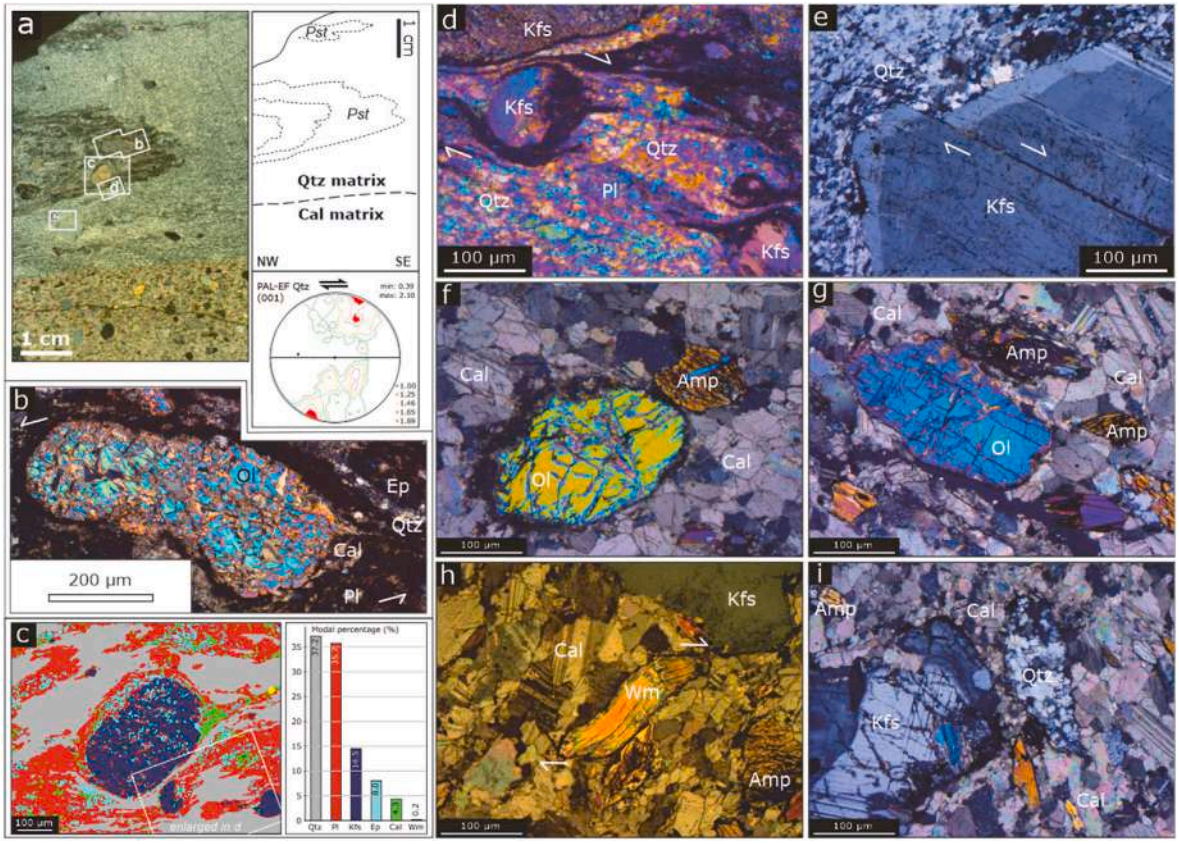

Fig. 5. Microstructural features of a mylonite (PAL-EF sample) from the Palmi Shear Zone: a) high-resolution thin section optical scan (crossed polarizers; Pst = pseudotachylyte) of the contact between tonalite (upper part) and skarn (lower part); inset figure shows quartz c-axes poles (dextral shear sense); b) fragmented olivine porphyroclast embedded in a microcrystalline calcite matrix; c) quantitative modal analysis of a domain with K-feldspar σ-porphyroclasts within fine-grained quartz-plagioclase matrix; d) quartz-rich microdomain at the base of the porphyroclast shown in (c); e) zoom-in on a book-shelf zoned K-feldspar porphyroclast in a quartz matrix; f-i) photomicrographs of deformed olivine (Ol), amphibole (Amp), white mica (Wm) and quartz (Qtz)| porphyroclasts in calcite-rich (Cal) matrix.

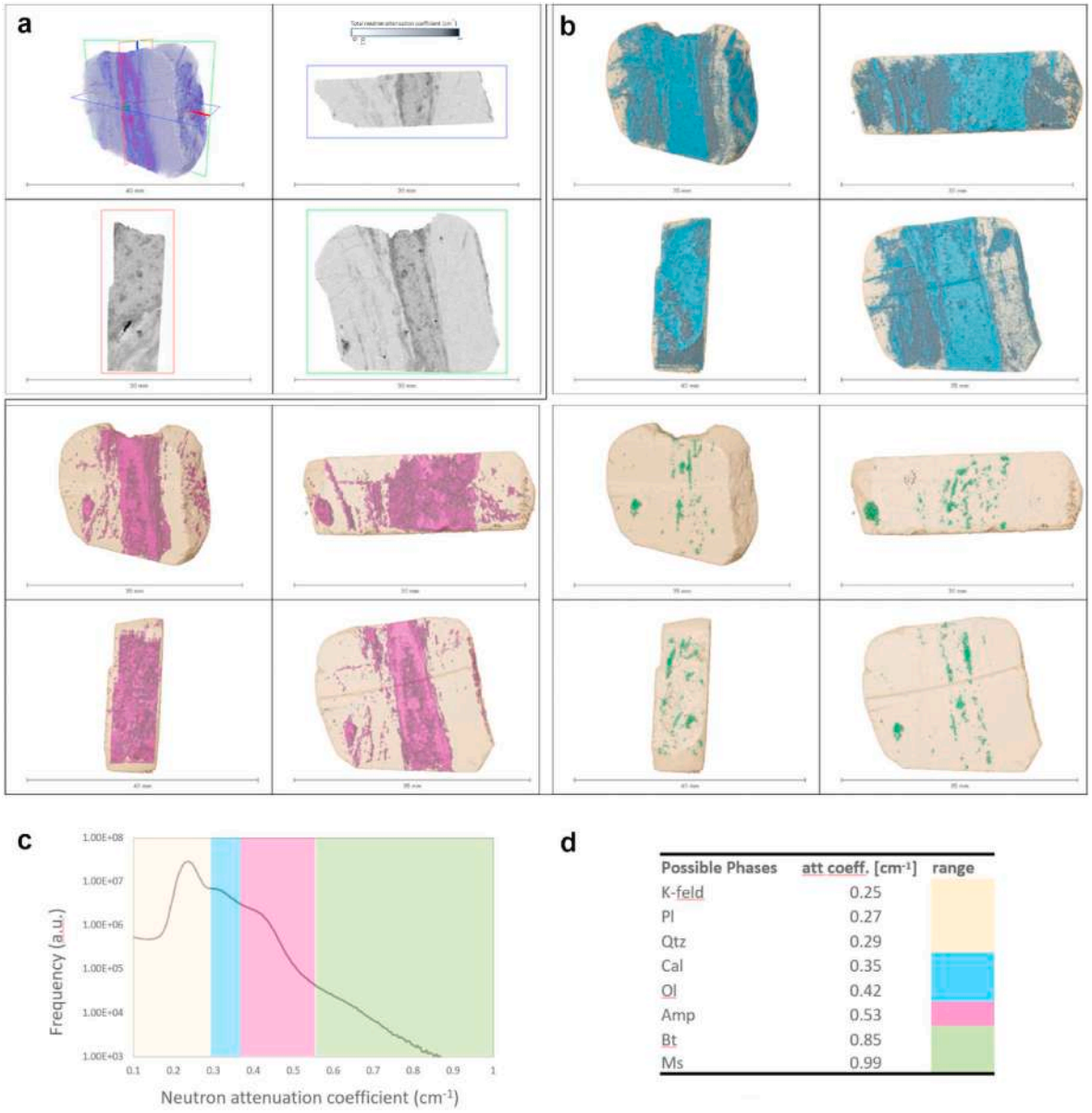

Fig. 6. Neutron tomography (sample PAL-EF): a) orthogonal slices through the reconstructed volume of the sample with location of the cropping planes indicated in the three-dimensional model; b) three-dimensional distribution of mineral phases shown in different directions-one perspective and three orthogonal ones. Phases are rendered based on the color code used to define the thresholding values adopted for the segmentation in c) the histogram of the frequency distribution of the neutron attenuation coefficients. The phases attributed to each segmented region in the histogram are reported in d). The attribution is based on the calculated theoretical neutron attenuation coefficients (at wavelength of 1.5 Å) of the major minerals identified by SEM. The segmented regions should be interpreted as an association of different minerals rather than single-phase. It should be noted that only one phase is attributed to the blue region. This is unlikely; therefore, the segmented region should be rather interpreted as volumes of mineral aggregates with different relative abundance. (For interpretation of the references to color in this figure legend, the reader is referred to the Web version of this article.)

ducts/software-em-3d-vis/avizo-software.html accessed on August 15, 2023).

Enhancement of the image quality of the tomographic data was achieved through noise reduction by an anisotropic diffusion filter coupled with an unsharp mask algorithm to reinforce the contrast at the edges. In the reconstructed tomographic slices composing the neutron tomographic stack, separation of the mineral phases/aggregates was obtained via threshold segmentation based on the difference in neutron attenuation intensities displayed as grey-tone values by different components. In the segmentation, each pixel in the slices is assigned to a label which describes the association pixel-mineral (e.g., Qtz, Kfs, Bt) within a defined range of grey-tone values. The segmented data were then further evaluated (Reddy, 2018).

The representative samples for neutron diffraction texture analysis were the same as used in the neutron tomography experiment, comprising a $20 \times 20 \times 7$ mm^3 slab. This specimen was measured using the constant wavelength neutron diffractometer KOWARI (Kirstein et al., 2009) at the Australian Nuclear Science and Technology Organisation (ANSTO, Lucas Heights, Australia). An incident neutron beam with wavelength of 2.5 Å was used to acquire neutron diffraction signals in a two-dimensional, position-sensitive area detector with approximately $15^\circ \times 15^\circ$ coverage. Overall nine quartz reflections, (100), (101)/(011), (110), (012), (111), (003), (202)/(022), (112) and (013), were extracted from the measured diffraction pattern on an approximately $3^\circ \times 3^\circ$ grid. Due to anisotropic shape of the sample, some corrections were applied to account for the anisotropic absorption effects

and avoid some pole figure distortions associated with this. Although some pole figures from other minor phases were available, only quartz texture (CPO) was of interest for the purpose of establishing shear sense (Fig. 5a). Data analysis was undertaken using the open-source software package MTEX (https://mtex-toolbox.github.io). The quartz CPOs were calculated as orientation density functions (ODF), constructed using a 'de la Vallee Poussin' kernel with 5° half-width in order to calculate the basal (001) pole figure of quartz.

4. Rock fabric analysis

Shear-related deformation along the PSZ is characterized by strain partitioning that is strongly influenced by a range of lithologies associated with high viscosity contrasts (Prosser et al., 2003; Festa et al., 2015; Ortolano et al., 2020). These rock types are mainly composed of mylonitic skarns, marbles, and metacarbonates, which act as the weaker phase accommodating most of the deformation within the shear zone (Prosser et al., 2003). Conversely, low-strain domains consist mainly of pegmatites, leucocratic dykes, and tonalites, which represent the more competent media, with migmatitic paragneisses in between.

Ortolano et al. (2020) provide a comprehensive study of the main lithotypes involved in the PSZ, focusing on meso-structural features and outcrop-scale investigations of deformation developed under greenschist facies conditions, as inferred from quartz recrystallization microstructures. Edge detection techniques (e.g., Visalli et al., 2021) confirm sub-simple shear deformation with an average 37% simple shear vs. an average 63% pure shear (with the latter component possibly overestimated, see Xypolias, 2010).

In this study, we selected a representative specimen of mylonitic skarn (PAL-EF, Figs. 5 and 6) characterized by interbedded layers of quartz-feldspar and calcite-rich matrix, which together with K-feldspars, olivine, amphibole, and scapolite often occur as porphyroclasts and are the most abundant mineral phases found in mylonites of the PSZ.

From a PAL-EF rock thin section, a micro-domain (2.85 μm × 2.22 μm sized) was selected and investigated with SEM-EDS to extract X-ray maps of major elements (Al, Ca, Cl, Fe, K, Mg, Mn, Na, P, Si, Ti) and BSE map. Using the software X-Min Learn (D'Agostino, 2023), such maps were processed with a pre-trained machine learning model to automatically identify the minerals. This particular micro-domain displays a central K-feldspar porphyroclast (14.48 wt%), surrounded by a dominant quartz-feldspar matrix (37.16 wt% and 35.74 wt% of quartz and plagioclase, respectively). Subordinate phases are epidote (8.0 wt%), calcite (4.30 wt%), white mica (0.17 wt%) and apatite (0.06 wt%).

The microtomography analyses confirmed the main assemblage observed in thin section and supported the domanial modal estimates obtained by means of X-Min Learn (D'Agostino, 2023) suggesting a complex micro-fabric given by the alternance of quartz-rich levels alternating to calcite-rich matrix with floating clasts of various mineral phases. Also, at microscale the microtomography results (Fig. 6c–d) confirm how the bulk rock rheology is controlled alternatively by calcite or quartz according to their modal abundances (Fig. 5c).

The skarns exhibit a mineralogical assemblage consisting primarily of calcite, K-feldspar, and quartz, with calcite being the most prevalent mineral and responsible for the bulk rheological behavior (Fig. 5f–i). At the microscale, calcite is found in high-strain domains within the matrix as cryptocrystalline aggregates that alternate with thin quartz layers (Fig. 5a–d-e). These domains delineate the mylonitic foliation (S_M), whose orientation is frequently perturbed by the existence of microfolds and is deflected around competent clasts, primarily composed of feldspar porphyroclasts. These clasts reveal brittle behavior and create σ - or δ -type fragmented porphyroclasts (Fig. 5b–e), indicating a dextral sense of shear (Fig. 5c–d). This shear sense is also shown by S-C structures identified in calcite-rich layers within ultramylonites (Ortolano et al., 2020).

The mylonitic migmatitic paragneisses comprise quartz, K-feldspar, plagioclase, biotite, amphibole, garnet, sillimanite, and white mica, with quartz dominating the whole-rock rheology. At the microscale, quartz grains display evidence of sub-grain rotation (SGR) and grain boundary migration recrystallization (GBM) (e.g., Ortolano et al., 2020), indicative of shearing under mid-temperature conditions. Feldspars exhibit brittle behavior as demonstrated by bookshelf-sliding structures (see Fig. 5e), which indicate a local sinistral sense of shear, although most of the kinematic indicators highlight a dominant dextral top-to-the SE shear sense (Fig. 5c–d). Micas are present both in the cryptocrystalline matrix defining the mylonitic foliation that wraps feldspar porphyroclasts, and in the form of larger mica-fish structures (Fig. 5h). The alignment of these structures suggests a pre-kinematic feature with a dextral sense of shear (see Fig. 5c–d, h).

Analogous to the paragneiss, quartz also regulates the rheology of the mylonitic tonalites and leucocratic dykes where K-feldspar and plagioclase, respectively, are the other major mineralogical phases. At the microscale, quartz forms ribbon-like structures, and the effects of SGR can be identified, while feldspar porphyroclasts display brittle behavior, often resulting in 'bookshelves' (Fig. 5e) with fractures infilled by a microcrystalline quartz matrix.

5. Field and aerial surveys

Structural data was collected from eleven stations positioned within the boundaries of the PSZ (Fig. 3; see Table 1 for location of each station). In this section, we summarize the spatial orientation of various planar and linear structures. In particular, we establish a strong correlation between field data collected by compass (both traditional and digital ones) and those inferred by 3D virtual outcrop models (Fig. 7). The calibration of orientation between field measurements and those created virtually from models produces good results with an accuracy of about 5°.

The key features observed in outcrops of the PSZ (Figs. 8–13) consist of a pervasive sub-vertical or steeply inclined mylonitic foliation (S_M) that generally trends E-W (Fig. 3). The exception to this is at Site 1 (Ulivarella reef, Fig. 8a–e) where the fabric is rotated and strikes NW-SE, becoming sub-horizontal on its southern portion (Fig. 9d–f). In addition, the mylonitic foliation contains a strong sub-horizontal to sub-vertical stretching lineation (L_M) that generally trends ESE-WNW.

An interesting aspect of the PSZ is the sheath-like geometry of both small- and large-scale folds (Fig. 9c–d). Of particular interest is a localized shear zone (ca. 2 m thickness) dipping to the SE at Site 7 (Fig. 14 and Supplementary Fig. S4) where migmatitic paragneisses intruded by a leucocratic dyke are deformed into a metre-scale fold (wavelength approximately 4 m). This weaker ductile boundary, preserved in a sea cliff, was identified from a boat and its orientation was only later derived via a virtual 3D model of the outcrop (Fig. 14a–e). The shear plane, which dips at a low angle when compared to the general subvertical mylonitic foliation, continues towards the SW and is visible at Site 8 where, using 3D VOM (Fig. 14h–n) it was possible to determine the orientation of structural elements (foliations, fold axes, axial planes, shear planes).

Structural data was collected from the different sites, including the orientation of foliations (n. 1078 data in total), which may also be reliably inferred from the 3D VOM (Virtual Outcrop Model), together with fold axes (n. 93), axial surfaces (n. 141), shear planes (n. 22), joints (n.118) and faults (n.15). Stereoplots of data from the single sites are shown in Figs. 8–10, 13, 14 whereas merged structural data sets are summarized in Fig. 7.

6. Kinematic analysis

A number of deformation phases (Table 2, Figs. 15 and 16) are recognized through structural analysis conducted in the field, and verified both in thin section and through drone imagery. The shearing related deformation, which has been interpreted to be of Alpine age based on ages reported by Prosser et al. (2003), can be summarized as

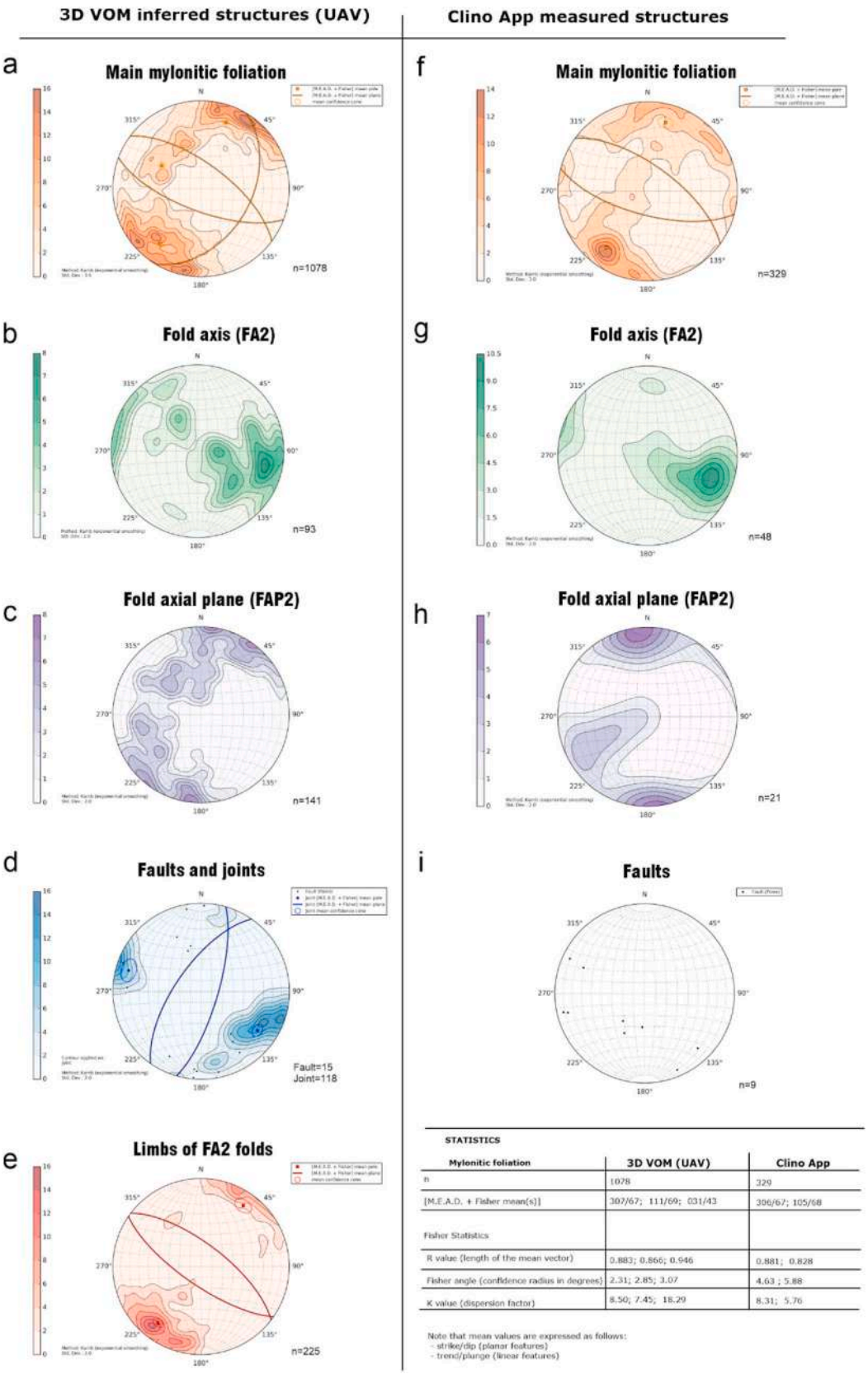

STATISTICS

Mylonitic foliation	3D VOM (UAV)	Clino App
n	1078	329
[M.E.A.D. + Fisher mean(s)]	307/67; 111/69; 031/43	306/67; 105/68
Fisher Statistics		
R value (length of the mean vector)	0.883; 0.866; 0.946	0.881; 0.828
Fisher angle (confidence radius in degrees)	2.31; 2.85; 3.07	4.63 ; 5.88
K value (dispersion factor)	8.50; 7.45; 18.29	8.31; 5.76

Note that mean values are expressed as follows:
- strike/dip (planar features)
- trend/plunge (linear features)

Fig. 7. Summary stereoplots of data (merged from the various sites) collected from all eleven sites by means of (a–e) 3D VOM analysis and (f–i) digital compass (ClinoApp Move; data are limited to directly accessible exposures). The inset table (in the lower right corner) shows a statistical comparison between data of mylonitic foliations collected with the two methods (values of attitudes are expressed in the right-hand rule and are referred to the statistical best fit circles – three main planes representative of 1078 data plotted in a, and two main planes representative of 329 data plotted in f).

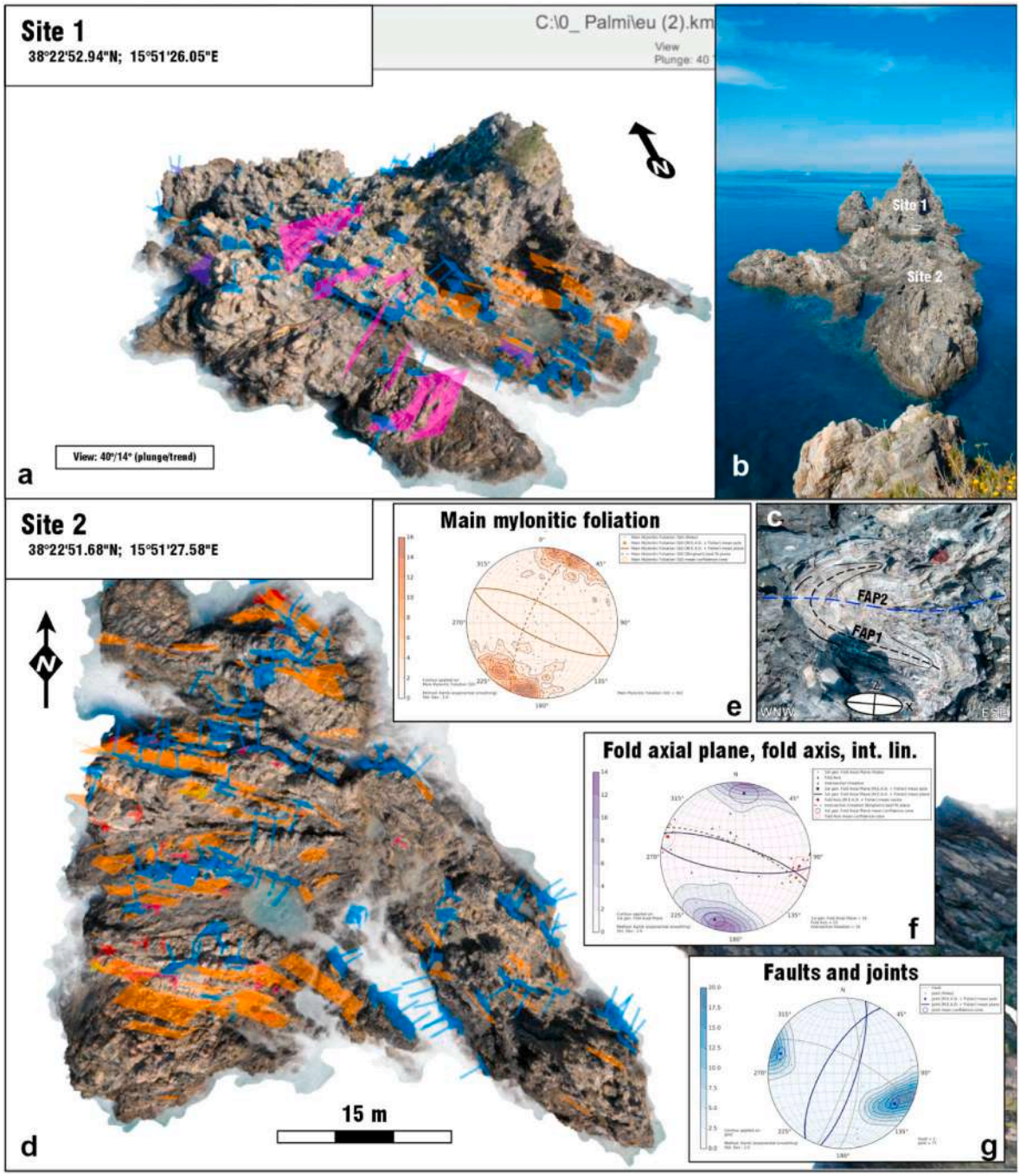

Fig. 8. a-b) Virtual outcrop model (VOM) of Sites 1 and 2 (see Table 1 for location) and their structural interpretation by means of the software GeoVis3D; planes are color-coded with respect to recognized deformational structures. c-g) VOM of site 2: c) type-3 fold interference pattern (Ramsay classification - FAP1 and FAP2 are axial planes of FA1 and FA2 folds, respectively; a qualitative representative section of the inferred strain ellipsoid is also shown); d) aerial zenithal view of Site 2 with interpreted structures; e-g) Cumulative stereoplots of Sites 1 and 2 showing: e) contoured mylonitic foliation (Sm; n.402 data); f) contoured fold axial plane (F2A; plotted n. 34 data) together with poles of fold axes (F1A and F2A; n.15 data); g) contoured brittle joints (n. 77 data), three fault planes are plotted as great circles (mainly NNE-SSW oriented). (For interpretation of the references to color in this figure legend, the reader is referred to the Web version of this article.)

follows.

- D1 shear zone activation (mainly sinistral strike-slip), sheath folds (FA1) ranging in size from a few centimeters (station No. 10 near the beach, Fig. 3a–e) to several meters (stations No. 7 and 11) develop together with asymmetric and near isoclinal intrafolial folds. Sinistral shear bands are developed (e.g., Fig. 11c and 12f).
- D2 shear zone reactivation with an opposite shear sense (mainly dextral strike slip) resulting in new oppositely verging folds (FA2) and sigmoidal clast interference patterns (Fig. 17); new dextral sigmoidal clasts can also develop (Fig. 16g–h). Progressive deformation tends to re-fold earlier sheath folds causing fold interference patterns (Fig. 8c). The continuous deformation and intense shearing deform the earlier fold hinges, which in turn behave as σ-type objects exhibiting dextral-shear kinematics (Fig. 9e and fg). Earlier en-echelon fold axes are also dextrally sheared (Fig. 11a).
- D3 folding (FA3) of the mylonitic foliation which is often subparallel to the earlier Hercynian foliation that also deforms the discordant

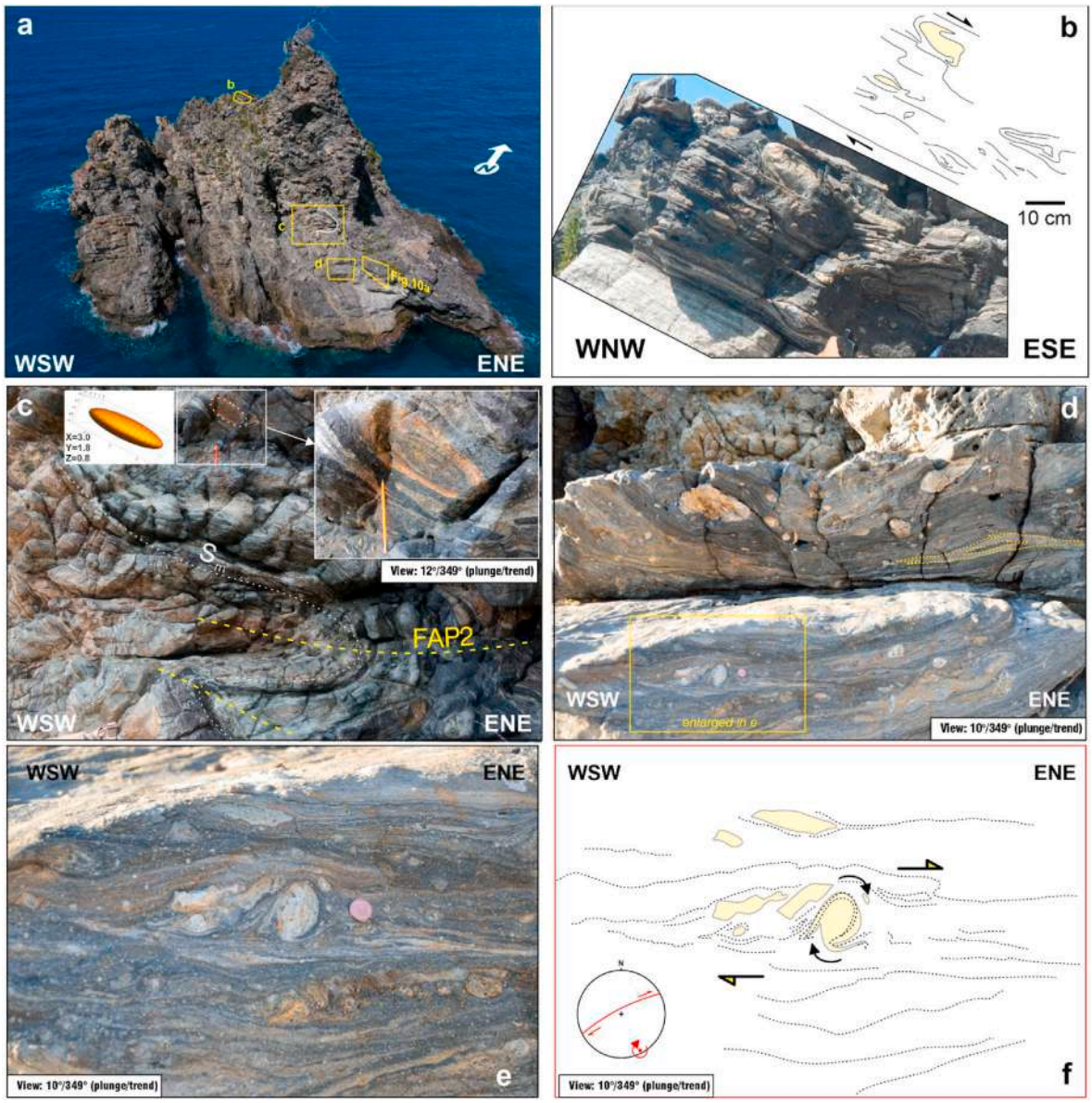

Fig. 9. a) Panoramic view of Site 1 (Ulivarella Stack); b) Ultramylonitic layer of migmatitic paragneisses and marbles (upper dark layer) with kinematic indicators (verging folds, rigid sigma- and delta-type clasts) overthrusting a pegmatitic light-colored centimetric lenses giving a top to the ESE sense of shear; c) sheath fold in the upper limb of a metric fold (FA2), the strain ellipsoid (values of 3.0, 1.8, and 0.8 arbitrarily assigned for X, Y, and Z axes, respectively) depicted only for qualitative aim, has been constructed by 'Ellipsoid' (Weisstein, 2013) by using the software Wolfram Mathematica v.13.2. (d) vertical surface of outcrop (for location see Fig. 9a) with a dextrally-sheared sheath fold and a lot of σ - and δ-type clasts displaying opposite shear sense; (e) complex winged δ-type clast indicating top-to-the-ENE shear sense; (f) interpretation of structures depicted in (e); the inset show a stereoplot with location of a clockwise vorticity axis compatible with the clast at the center of the picture, the red great circle represent the outcrop subvertical surface depicted in (e) (see Fig. 10g for details and conceptualized scheme). (For interpretation of the references to color in this figure legend, the reader is referred to the Web version of this article.)

contacts of the late Hercynian dykes (e.g., site 7 on Fig. 3a and 14a-e). The almost coeval development with the (FA3) folding of a NE-SW oriented thrust, compatible with a general dextral shearing zone boundary, occurred at the base of a narrow mylonitic shear zone a few meters thick within an intensely ductile deformed level of marbles, showing predominantly dextral kinematic indicators (site 8, Fig. 14g–n).

- D4 is characterized by brittle deformation with the occurrence of high-angle normal faults (Tripodi et al., 2018) and pseudotachylytes formation (Grande et al., 2009).

According to Festa et al. (2015), the PSZ was active during Early Eocene sinistral transpression, with a dominant left-lateral shear sense and rare evidence of dextral kinematics. However, Ortolano et al. (2020) proposed a dominant dextral shear direction for the same Alpine shear zone.

Several kinematic indicators, such as asymmetric verging folds, non-cylindrical folds, interference folding patterns, synthetic C′-type shear bands, and, most commonly, rigid δ- and σ-type clasts of pegmatites/leuco-dykes were identified on vertical outcrop faces at various sites (Figs. 13–15). In particular, clockwise (CW) rotations are observed on a sub-vertical ENE-WSW oriented plane, whereas counter or anti-clockwise (ACW) kinematic indicators are observed on a sub-vertical WNW-ESE plane. By plotting a stereoplot of the exposed outcrop surfaces and interpreting the kinematic indicators, it can be established that a top-to-NNE shearing occurs on the sub-horizontal mylonitic foliation (Fig. 10g); nevertheless, mainly sub-horizontal stretching lineations orientations collected at this site are subparallel to a ESE-WNW

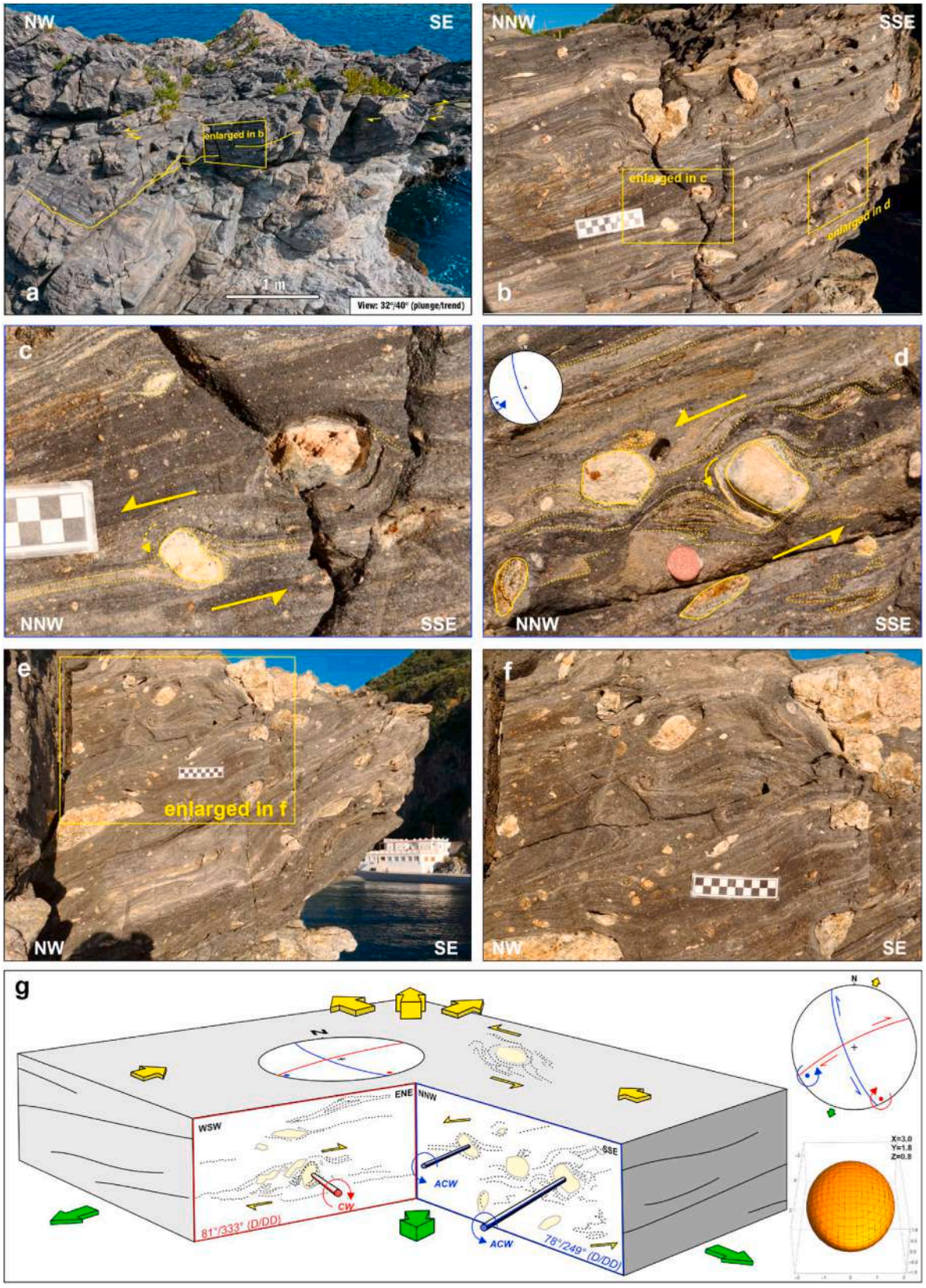

Fig. 10. a) Site 1 exposure near the volume shown in Fig. 9d (see Fig. 9a for location); b-f) Mylonitic foliation in skarn with multiple rigid clasts of tonalite/pegmatite/aplite (centimetric scale or coin for scale bar); g) Summary kinematic interpretation and schematic stereoplot of rigid clasts shown in Fig. 9e–f and 10c-d. The strain ellipsoid in the lower right corner (values of 3.0, 1.8 and 0.8 arbitrarily assigned for X, Y and Z axes, respectively) was constructed by 'Ellipsoid' (Weisstein, 2013) using Wolfram Mathematica v.13.2 software. Blue and red colored sticks represent the orientation of vorticity vectors of clasts (CW, clockwise spin; ACW, anticlockwise spin). Yellow and green arrows qualitatively represent the orientation of shear flow lines at the upper and lower planar boundaries of the investigated rock volume, where rigid clasts are characterized by both clockwise (pole, large circle, arrows in red color) and counterclockwise (pole and arrows in blue color) rotation. (For interpretation of the references to color in this figure legend, the reader is referred to the Web version of this article.)

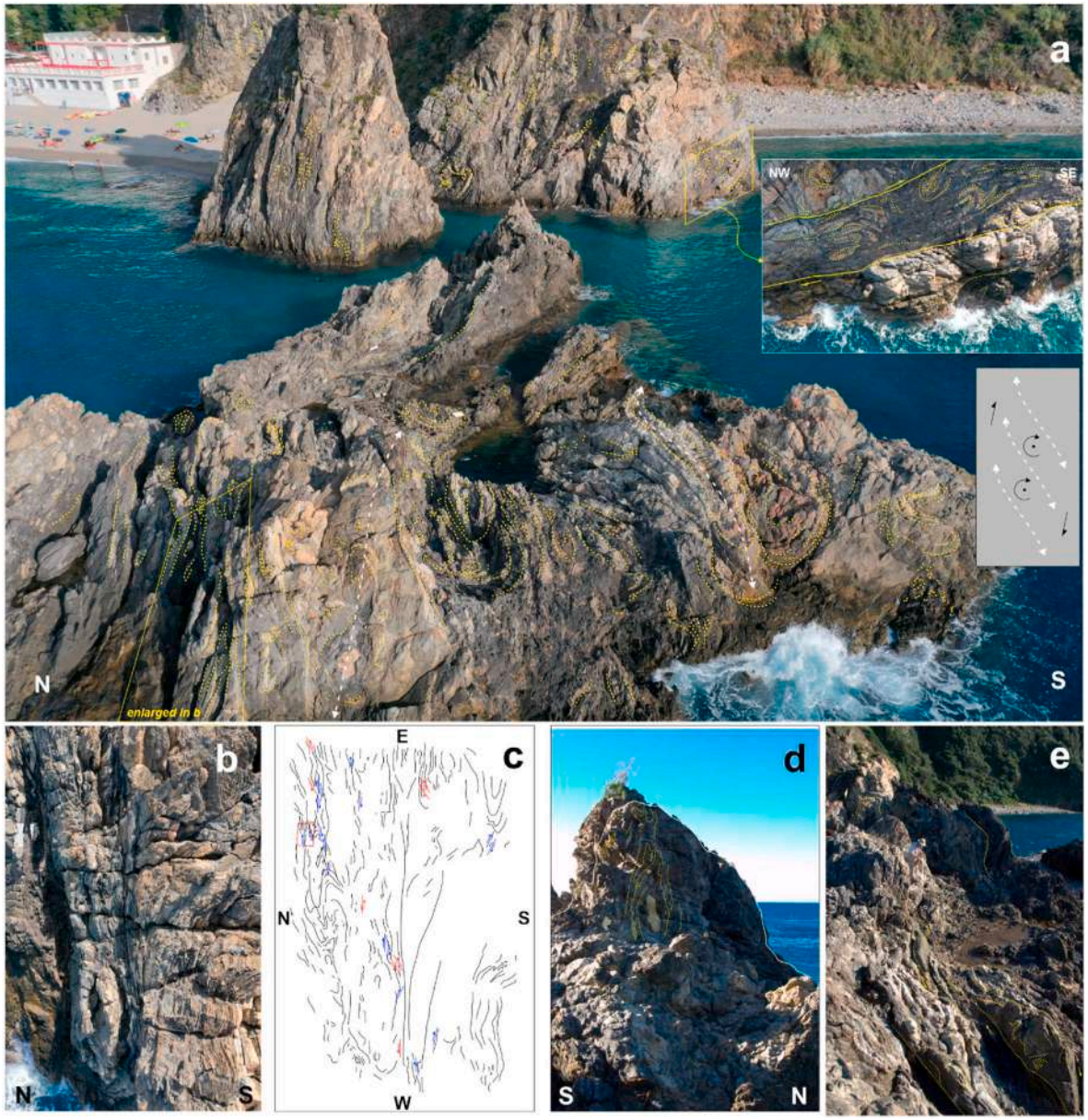

Fig. 11. a) Aerial view of Sites 2–5 (see Fig. 3a for locations); b) top view of a portion of outcrop shown in (a); c) interpretation of mesostructures in (b) (in red and blue color are marked sinistral and dextral shear planes, respectively); d-e) boudins of rigid leucocratic clasts and fish-shaped pegmatites at Site 2. (For interpretation of the references to color in this figure legend, the reader is referred to the Web version of this article.)

direction. Further analysis at Site 1 reveals some sinistral kinematic indicators on horizontal surfaces across the NNW-SSE trending vertical mylonitic foliation (Fig. 12). Numerous dextral kinematic indicators were also identified at Site 1 on vertical ESE-WSW trending mylonitic foliations (Fig. 9b). In light of these observations, it can be deduced that, at least at Site 1, there are steep ESE-WNW trending shear zones with dextral kinematics that are also compatible with the observations from Site 2 (Fig. 11a).

7. Discussion

7.1. Distinguishing shear sense in high strain zones

Defining the general sense of shear in high strain zone, and the PSZ in particular, remains potentially difficult due to a number of concomitant factors that are discussed below.

- *Contrasting kinematic indicators*: Confusion in determining shear sense may reflect the occurrence of numerous contrasting (dextral/sinistral) kinematic indicators, even when observed on the same face of an outcrop (Fig. 13e–f). In such situations, flow apophyses delimiting zones with δ - and σ-type clasts, marking forward or backward rotation with respect to the flow of the shear zone, can occur (Xypolias, 2010; Fossen and Cavalcante, 2017; Fossen et al., 2019). This may be related to pure-shear dominated flow within the PSZ with pure shear and simple shear forming ca. 65% and 35%, respectively (Ortolano et al., 2020).
- *Contrasting flow geometries*: Ductile flow geometries may shift from monoclinic (Passchier, 1998) to triclinic symmetry due to different rock types (with strong pre-existing fabrics) being involved in shearing, as well as the mutual influence of shortening and shearing components. Nevertheless, it should be noted that sheath folds (which are relatively common in the PSZ) are not usually associated with triclinic symmetry (Lin et al., 1998).

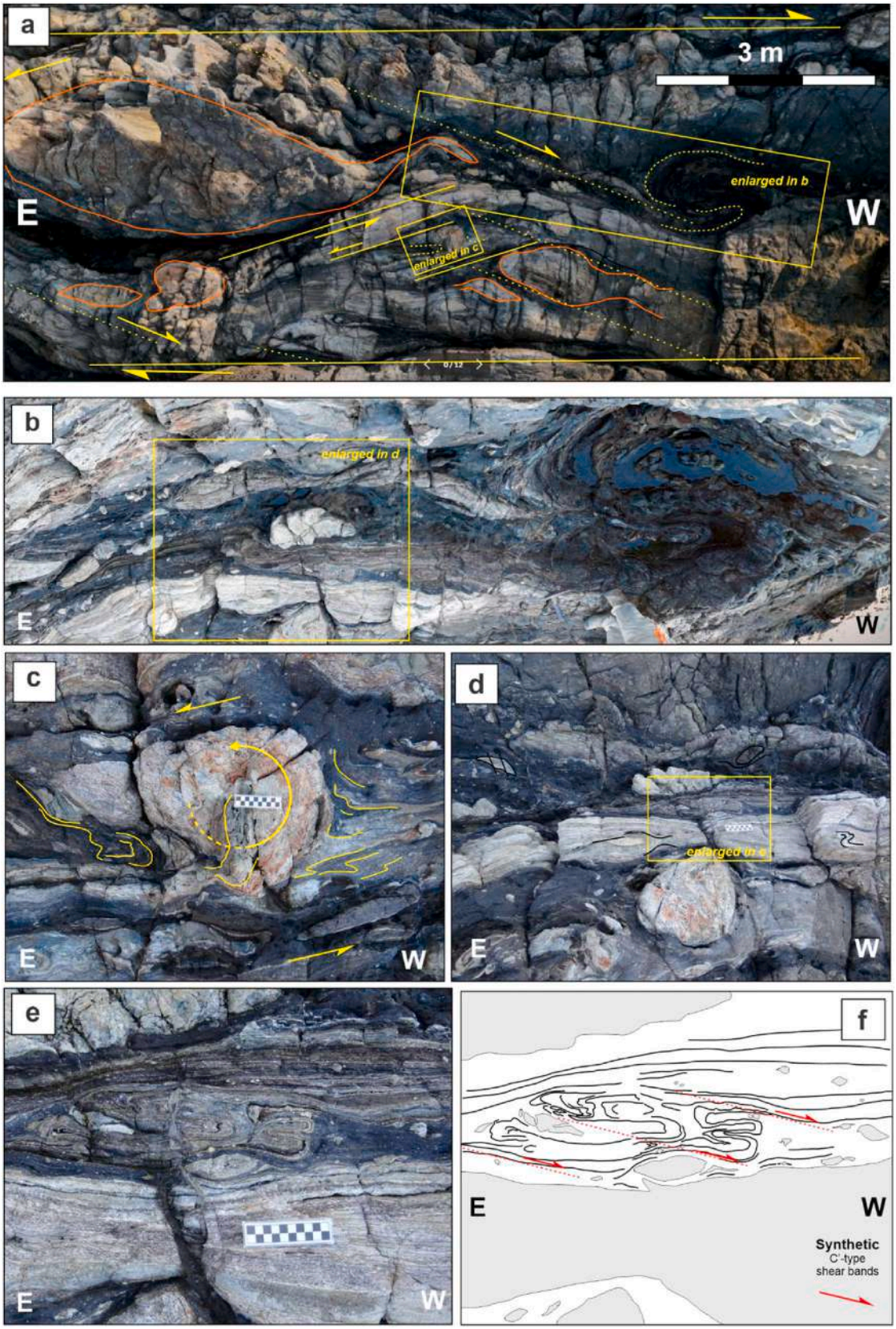

Fig. 12. Polyclinal folds (FA1) produced by progressive deformation under general shear (sub-simple shear) conditions. a) aerial view of sinistral and dextral shear planes; b) fold (FA1) indicating a dominant sinistral shear sense; c) competent clast of pegmatite (flower-type structure?) suggesting sinistral shear sense; d) detail of (b) where a dextral (E-W oriented) shear plane dislocate the pegmatite near the center of the picture; e) interference fold pattern and f) interpretation of mesoscopic structures as synthetic dextral C′ type shear bands.

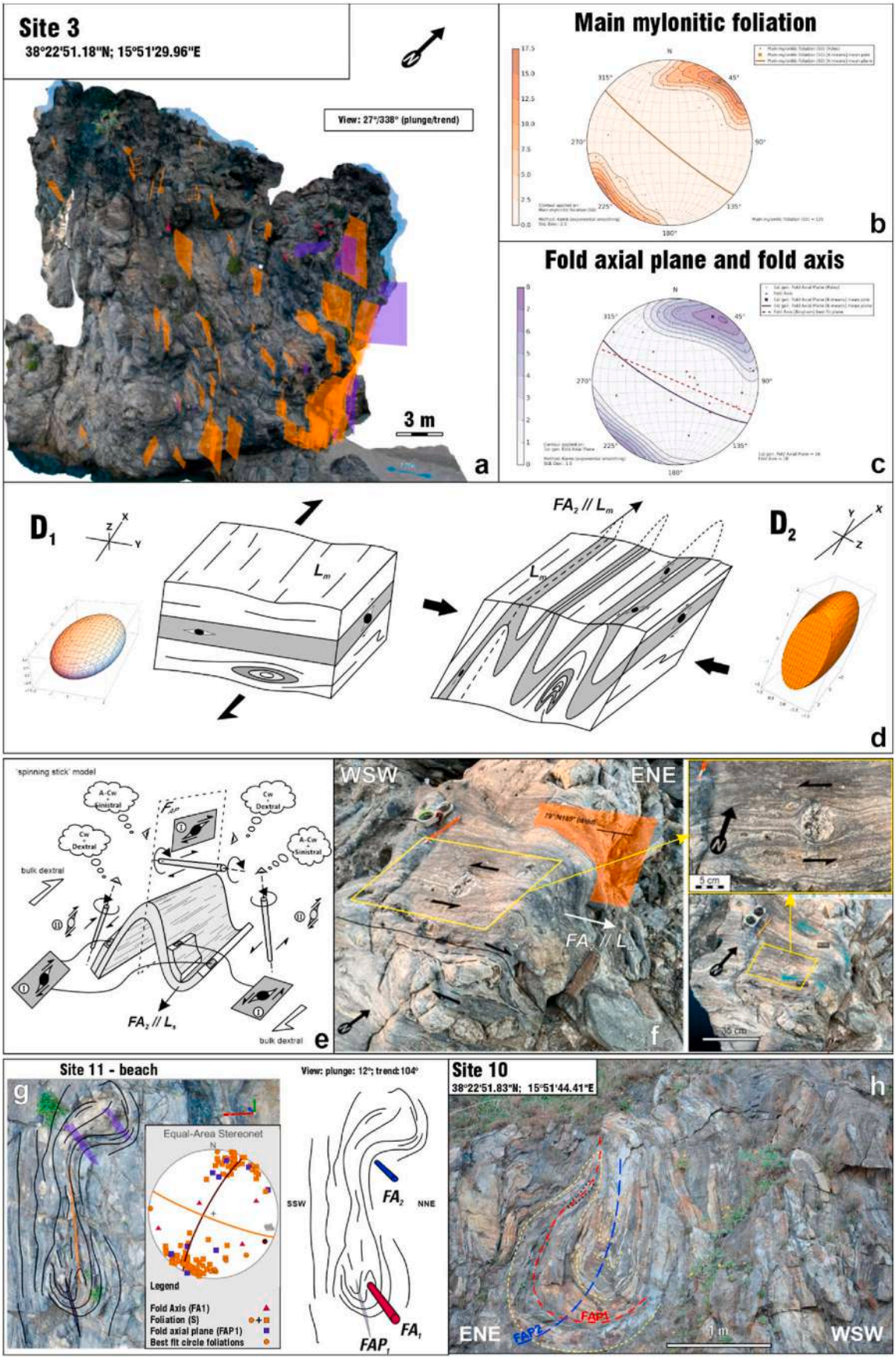

(caption on next page)

Fig. 13. a) 3D VOM and mesoscopic structures recognized at Site 3; b-c) Stereoplots of mylonitic foliation, fold axial plane and fold axis inferred from the digital 3D virtual outcrop model (GeoVis3D software); (d) Conceptualized model of D1 and D2 deformational phases (strain ellipsoids shown are only for qualitatively purposes; abbreviations: L_m = stretching lineation; FA2 = syn-D2 fold axis); e) Schematic sketch conceptualizing the 'spinning stick' model: a ductile high strain zone with dominant bulk dextral shear generates folding of the mylonitic foliation with the hinge parallel to flow direction. This results in apparent opposite senses of rotation (CW clockwise vs ACW anticlockwise) of the kinematic indicators (I and II indicate pre- and syn-to late-folding sigmoid clasts, respectively) as occurs in many outcrops of the PSZ; (f) δ - and σ- (sigma) type clasts showing opposite shear senses (the lower right inset is a 3DVOM reconstructed by LiDAR portable sensor); (g) Interference fold pattern at Site 11 (near Site 3; see map of Fig. 3 for location) between FA1 and FA2 folding systems; (h) Outcrop view at Site 10 (Malopasso location) with clear interference fold patterns (Type 3 Ramsay) in metacarbonates alternating with mylonitic migmatitic paragneisses.

- *Contrasting minor shear zones*: Multiple minor shear zones with opposite shear sense may develop subparallel to the margins of the main shear zone boundaries that are deflected by lenses of more competent material (pegmatites and leucocratic granitoid dykes) within the finer-grained weaker marbles and Ca-silicates that readily deform plastically. Some such secondary shear planes have been interpreted as type-C′ shear bands (Fig. 12e–f) from field observations supplemented by traces of mylonitic foliation interpreted from UAV photographs.
- *Minor fold interference*: Sheath folds of the mylonitic foliation are transposed and refolded by the progressive syn-shear deformation phase (e.g. Alsop, 1994; Forbes et al., 2004), resulting in fold interference patterns that transpose the original relationships. Such fold interference patterns vary from Ramsay type 2 to 3.
- *Inherited folds and fabrics:* The pre-shearing structural features of the various protoliths to mylonites, consisting of migmatites, pegmatites, marbles and skarns, may have preserved some remnants of earlier structures, such as migmatitic fabrics or previously folded pre-Alpine foliations. In the PSZ, this is usually characterized by alternating segregated leucosomatic melts and restitic layers, which add complexity to the overall rock fabric.

7.2. Scenarios to explain opposing kinematic indicators in shear zones

There are several possibilities that could help explain the opposing sense of shear observed in the PSZ.

- *Sections oblique to shear*: Sections should always be interpreted in the sense of shear plane that is normal to the foliation and parallel to the transport lineation. However, many natural sections are oblique to this perfect plane, resulting in apparent reversals in shear sense. Extreme caution needs to be exercised where the available section is oblique to the true sense of the shear plane, and observations should be combined with others from differently oriented planes to determine the true shear sense (e.g. Fig. 10g).
- *Mechanical heterogeneity around rigid clasts*: Marques and Burlini (2008) conducted tests on analogue materials (a mixture of 70% halite and 30% muscovite) and showed that deformed, ductile rocks behave like a continuum at the macroscopic scale, allowing the analysis of the rotational behavior of rigid inclusions via fluid mechanics. The sense of shear is altered at the periphery of a single rigid body, as occurs in shear layers around vortex tubes in fluids (e.g. Ma et al., 2022). Asymmetric tails around clasts could also be indicative of lateral sense of shear (Marques et al., 2007). Opposite senses of shear observed in the PSZ are considered to potentially reflect the rheological contrast between more competent material and a weaker matrix. The more competent bodies comprise both mega-clasts of tonalites, pegmatites, or isoclinally refolded layers of migmatites (Fig. 12b–d), which generally form sigmoidal objects. The weaker matrix consists of fine-grained marbles and Ca-silicate mylonites. Such competency controls should be considered when analyzing larger portions of outcrop, as well as single folded layers. It should be noted that a misinterpretation of winged inclusions, known for their high viscosity contrast between clast/matrix (Grasemann and Dabrowski, 2015), could mislead the evaluation of the shear zone's kinematics. Indeed, larger clasts may have significant effects on the surrounding volume similar to the Coanda effect (Cicolin et al., 2023) typically identified in fluid mechanics in the proximity of vortex tubes formed during shear flow streaming (Ma et al., 2022). Vortices in the PSZ are represented by rolling hinge structures or spiral-like folds (e.g. Fig. 16; Gorbunov and Balagansky, 2022) of competent material (pegmatite layers) developed in the skarn. Opposing clockwise and anticlockwise vortexes in the tails of an 'obstacle' (analogous to harder clasts of leucocratic dyke within the skarn or calc-silicate marbles) to the laminar flux may be generated. The result is an apparent reversal in shear sense as defined by kinematic indicators if only this small portion of the outcrop is considered.
- *Interference between rigid clasts*: Adjacent rigid clasts may interact with one another, forming strain shadow zones (Mandal et al., 2001; Griera et al., 2013 and references therein) to create local interference and apparent reversals in shear. This situation occurs frequently in the PSZ from outcrop to thin section scale since clasts of 'harder' material (quartz-rich layers, tonalite tectonic lenses, or aplites/-pegmatite folded dykes) act as rigid bodies floating in the calc-silicates rocks (Fig. 10). Winged clasts of larger size could have meter-sized elongated tails subparallel to the mylonitic foliation, where smaller centimetric harder clasts may rotate (clockwise or anticlockwise) with respect the general shear sense of the bigger clast wings. Moreover, high-strain bands (or 'stripes') form a layering visible at outcrop scale highlighted by slight color difference in skarn lithologies (Fig. 10f) subparallel to the main mylonitic foliation (Fig. 18a–D2 inset V) and local shear planes can interact with each other (e.g. Gardner et al., 2017).
- *Ductile extrusion*: Shear sense will reverse when comparing the opposing margins (top and bottom contacts) of an extruding wedge (Tóth et al., 2023). This also applies to differential movement in the cores of sheath folds across a range of metre-km scales (e.g. Alsop, 1994; Alsop and Holdsworth, 2012).
- *Variation in rates and values of simple shear*: Shear sense will reverse if rates of simple shear vary with some areas locally 'lagging behind' the general rates of shearing (as if a playing card sticks in a shuffled deck of cards). Variation in the value of simple shear (compared to pure shear) may result in sub-simple shear regimes with the mutual occurrence of forward and backward rotating clasts, as previously established for the PSZ (e.g. Festa et al., 2015; Ortolano et al., 2020).
- *Folding of shear sense indicators:* Shear sense will apparently reverse if the mylonitic foliation is later folded around transport-parallel fold hinges. While fold hinges that form at high angles to transport do not create reversals in shear sense, many fold hinges develop parallel to shear due to variations in rates of movement or 'flow perturbations' within high strain zones (e.g. Alsop and Holdsworth, 1993, 2002, 2004; Alsop et al., 1996). Kinematic indicators with opposing shear sense on the same face of the outcrop may thus relate to isoclinal folding of the mylonitic foliation, with fold axes parallel to the stretching lineation L_M as observed in the PSZ - see Fig. 13d–e and stereoplots in supplementary materials). This implies that opposite shear directions could be photographed depending on the outcrop surface on which observations are made (see the 'spinning stick' model of Fig. 13e). According to this model (the conceptualized scheme is shown in Fig. 13d–e), the mylonitic foliation is folded, giving rise to folds with normal limbs (those on the left of Fig. 13e) and reversed limbs (those on the right of the figure, where pre-folding clasts show apparent sinistral movement). Based on the

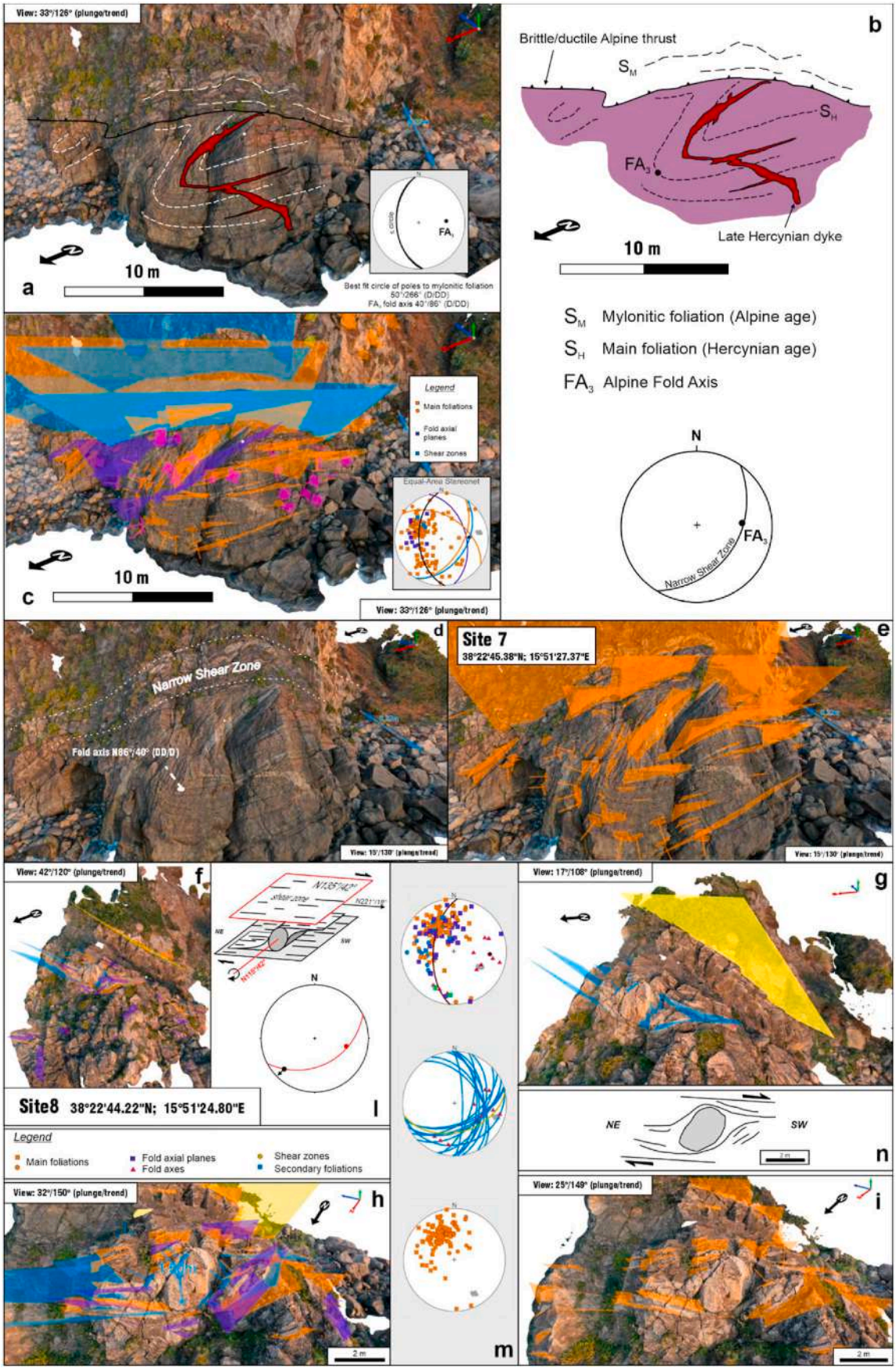

(caption on next page)

Fig. 14. a) 3D VOM and mesoscopic structures at Site 7 together with stereoplots of structural data; b) structural interpretation of Site 7: a metric wavelength syn-D3 fold (FA3 oriented N86°/40° as dip direction/dip notation) also affecting a late-Hercynian pluri-centimetric thick leucocratic dyke crosscutting earlier Hercynian foliation; c) virtual orientation of planes and lines in the 3D VOM: the light blue colored planar surface has been interpreted as a ductile SE-dipping high strain zone (see d) evolving to a brittle thrust in mylonitic skarns; d) overview of Site 7 showing a SE dipping (Alpine?) narrow shear zone; e) same view of (d) showing spatial interpretation of foliations; (f) 3D VOM of Site 8 with perspective view of foliation planes; (g) 3D VOM showing the upper part of the outcrop at Site8 where a narrow shear zone (yellow plane); it is the same shear zone exposed also at Site 7 (see b-d) continuing here a few meters above a large sigmoid clast (light blue planes here depicted are subparallel to clast tails suggesting dextral shear sense); h-i) Detailed view of leucocratic rock large clast shown in (g); and mesoscopic structures at together with stereoplots of structural data; l) Sketch of the large leucocratic rigid sigmoidal clast (see g-i) with tails parallel to a SE-dipping shear plane (red circle in stereoplot; oriented N135°/42° in DD/D, i.e. dip direction/dip notation; red pole oriented N115°/42° DD/D is the inferred hypothetical rotation axis of clast, black arrow in the stereoplot indicates a top-to-the-SW sense of shear); m) Stereoplots showing orientations of the recognized structures (top = poles to various surfaces, see legend for more details; middle = planes of FAP2 fold axial planes + FA2 fold axes; bottom = poles to mylonitic foliation); n) interpretation of the mega-sigmoid clast shown in (i)... (For interpretation of the references to color in this figure legend, the reader is referred to the Web version of this article.)

Table 2
Deformational phases and related structures.

Deformational phase	Related mesoscopic structures	Site N.	Supposed age
D1 – Shear zone activation (mainly sx shear sense)	Intrafolial verging folds, sheath folds (FA1), sinistral shear bands	1, 2, 10	Hercynian?
D2 – shear zone reactivation with opposite shear sense (mainly dx shear sense) and compression	Folds (FA2), dextral shear bands, interference patterns, development of new dextral sigmoid clasts	2, 4, 8, 9, 10, 11	Alpine?
D3– Folding evolving to ductile-brittle thrusting	Metric wavelength folds (FA3); Top-to-the-NW brittle-ductile thrust and pseudotachylytes formation	1, 2, 6, 7, 11; 3, 4, 7, 8	Alpine
D4 - Faulting	Normal faults – NNE-SSW Scilla-Bagnara fault system	1, 2, 4, 5	Alpine

structural data collected (see stereoplots of Fig. 7b–g), at least in Sites 1, 3, 10 and 11, many fold axes (FA2) are subparallel to the stretching lineation (Lm), possibly causing the occurrence of apparent sinistral shear sense indicators (pre-folding clasts) at these sites due to folding, within a volume characterized by a dominant bulk dextral shear.

- *Flexural flow folds and shear*: Shear sense will be the opposite to the bulk kinematics if a component of flexural shear accompanies rotation of (pre-existing?) fabrics into shear zones (Hippertt and Tohver, 2002). Similarly, flexural flow folds in which the fold core translates at different rates to limbs may be associated with reversals in shear sense across the axial plane.
- *Shearing events are of different ages*: The above interpretations for reversals in shear sense assume progressive deformation. However, it may be entirely possible that the preserved shear sense is in fact of different ages (e.g. Hercynian and Alpine etc.). If a bulk dextral shear zone is characterized by progressive deformation, the new dextral kinematic indicators (example V in Fig. 18a–D2) will be superimposed on sinistral kinematic indicators that formed prior to folding (example III-D1 in Fig. 18a). Several examples of interference deformation patterns (Finch et al., 2022) have been detected in the PSZ (examples III-D2 Fig. 18a).

There are many other cases where deformation within a shear zone migrated both spatially and temporally giving rise to domains of older shear zone fabrics intercalated with zones of localized reworking (e.g. Reddy et al., 2003). Their data indicate for the western Alps region a complex kinematic history involving both crustal shortening and extension within the internal zones of the Alpine Orogen (Reddy et al., 2003). The unravelling of different aged deformation requires careful field observations both within and outside of high strain zones (Fossen et al., 2019), combined with targeted isotopic age constraints.

The PSZ is characterised by good exposures, but often close to the coast with very steep cliffs, and the use of UAVs was very useful to integrate the dataset of structures to be collected. Using aerial photographs, we detected for the first time in the Palmi area a dextral narrow shear zone at two different sites (site 7, Fig. 14b–d; and site 8, Fig. 14g–n) with a fairly homogeneous SE dip (Fig. 18), which we related to a syn-to late-D3 thrusting Alpine phase, compatible with the sketch shown in Fig. 18b.

We recognized both sinistral and dextral kinematic indicators in the studied outcrops, and we speculate that some of these structures (Fig. 17; Grasemann et al., 2003, Grasemann and Dabrowski, 2015) suggest a potential reverse kinematic evolution from earlier sinistral (D1) to late dextral (D2) shear direction (Fig. 18a), localised on sub-vertical, roughly E-W oriented planes.

In summary, sinistral sigmoidal kinematic indicators are observed at outcrop, and are overprinted by subsequent dextral shear bands (Fig. 11b–c, 12). The dextral shear was also confirmed by the distribution of c-axis quartz grains from a mylonite collected at the Palmi beach (Fig. 5a; Site 11 in Table 1). Typically, sigmoidal kinematic indicators are defined by elongate clasts, and resemble microstructures studied by Finch et al. (2022). These observations suggest that at least two episodes of deformation, with opposing shear sense, have developed in the PSZ. At least the last phase of shearing could be attributed to the Alpine orogeny.

There are, however, still many unanswered questions about the kinematic history of the PSZ (e.g. age of the D1 deformation episode? Variscan or Alpine?) and further geochronological studies are required. Prosser et al. (2003) argued, on the basis of Rb-Sr isotope exchange in biotite, that recrystallization associated with Alpine deformation is strictly controlled by localised shearing, since biotite separates from mylonitic granitoids gave ages of 51 ± 1 and 56 ± 1 Ma, corresponding to the early Eocene, whereas biotite separated from a sample of augen gneiss (collected near Taureana beach northward with respect the PSZ) not affected by Alpine deformation gave an age of 253 ± 4 Ma. However, the collection of new structural data using detailed 3D virtual outcrop models and the identification of interference structures has allowed at least parts of the multiphase tectonic evolution of the PSZ to be delineated and will contribute to a better understanding of crustal-scale regional high strain zones to guide future studies.

8. Conclusions

The multiscale investigations of geological structures in the crustal-scale Alpine Palmi Shear Zone outcropping along the well-exposed coastline highlight the importance and implementation of multiple survey techniques to successfully collect and interpret geological and structural data.

The comparison of the structural dataset inferred by VOMs, with manually collected foliation and lineation orientations display a remarkably good match (differences < 5°). This correlation permits the area of analysis to be extended to areas that are inaccessible or unsafe, characterized by very steep outcrop surfaces or potentially dangerous cliffs. Such cliffs display clear well exposed structures and may be mapped with a UAV that acquires significant new data in a few minutes.

The approach taken in this study, based on a strong mixture of

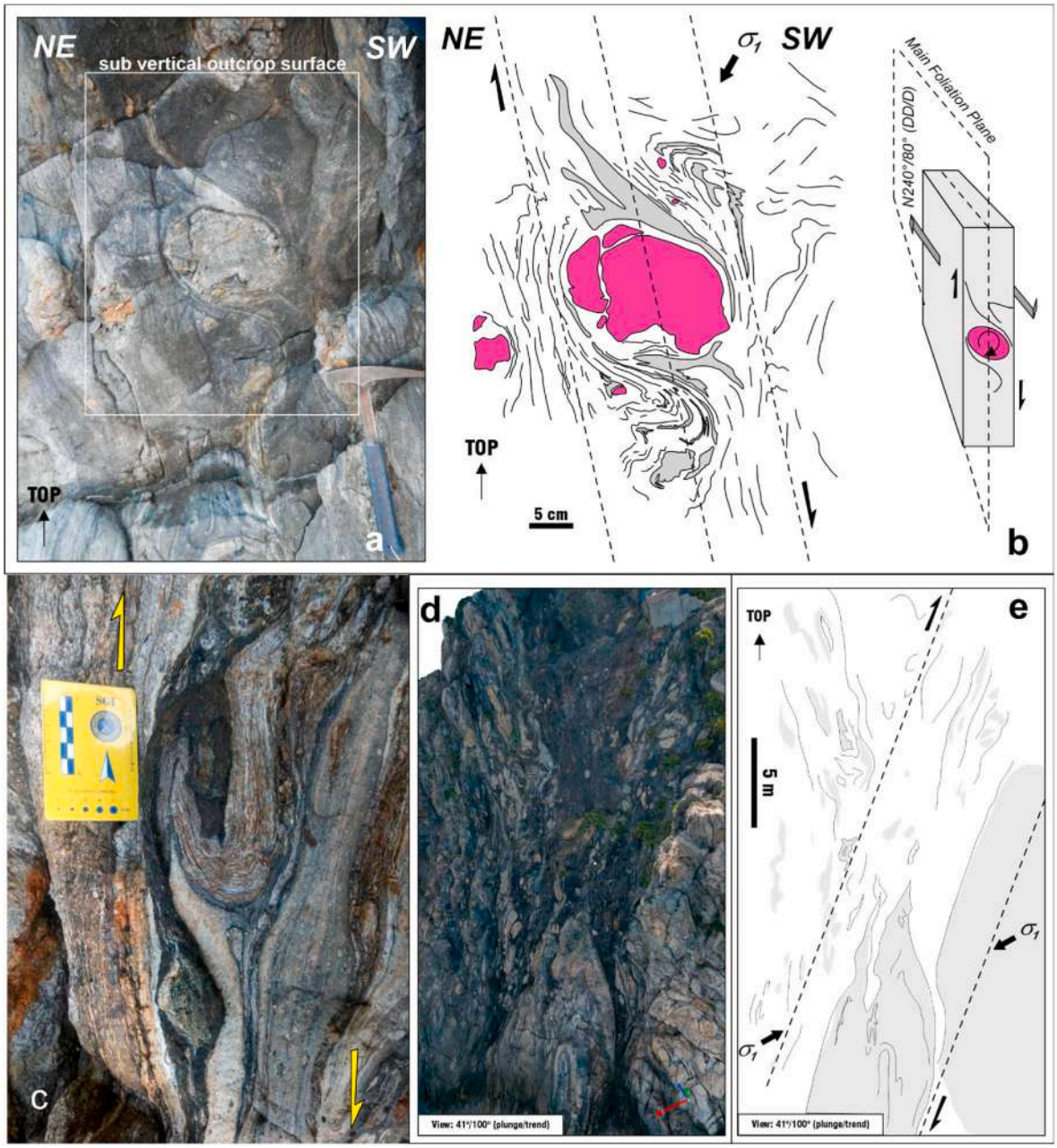

Fig. 15. a) δ -type clast of leucocratic dyke indicating dextral shear sense on subvertical mylonitic foliation at Site 4; b) interpretation of photo depicted in (a); c) mesoscopic appearance of folds developed due to the high viscosity contrast between skarn and migmatitic gneiss interlayered with a leucocratic lens (dextral shear sense); d-e) steeply dipping outcrop surface at site 4 (dextral shear sense).

classical (hand held compass measurements of structural orientations, direct "in situ" observations, and microfabric/micropetrography) and modern techniques of digital mapping such as VOM, reconstructed by means of aerial or digital LiDAR surveys, constitutes a natural evolution of the traditional geological field survey. This robust new approach is consolidated in a few geological departments during field classes and is likely to become the standard for future generations of field structural geologists.

It is noteworthy that 3D VOMs provide the possibility, albeit virtual, of reviewing different orientations of an outcrop according to perspectives chosen by the user. This is something that is otherwise not possible from simple photos (although they are oriented) unless one returns to the field. If the object of study is located in a remote area, having virtual support of this type recreates the conditions that the geologist is accustomed to facing on the ground, and with the opportunity can 'fly over' the site with previously unseen perspective views. Consequently, new structures that had not been noticed in the course of earlier surveys can be identified, and possibly selected for future exploration or targeted sampling.

The PSZ has an intricated deformation history since multiple folding phases and several shearing patterns have been preserved in the rock record. It is worth noting a minor component of shearing developed on subvertical exposure surfaces too (Fig. 16a–c, f) recorded by rigid clasts of various sizes (e.g. Fig. 15b) as well as flower-type fold or vertical extrusion 'squeezing' structures (Fig. 18a–D2 inset III). These structures confirm a general shear deformation (Festa et al., 2015; Ortolano et al., 2020) was active in the PSZ.

Dextral shearing firstly reported for the PSZ by Ortolano et al. (2020) has been recognized and confirmed from microscale (quartz c-axis pattern) to outcrop scale thanks to en-echelon trains of near isoclinal

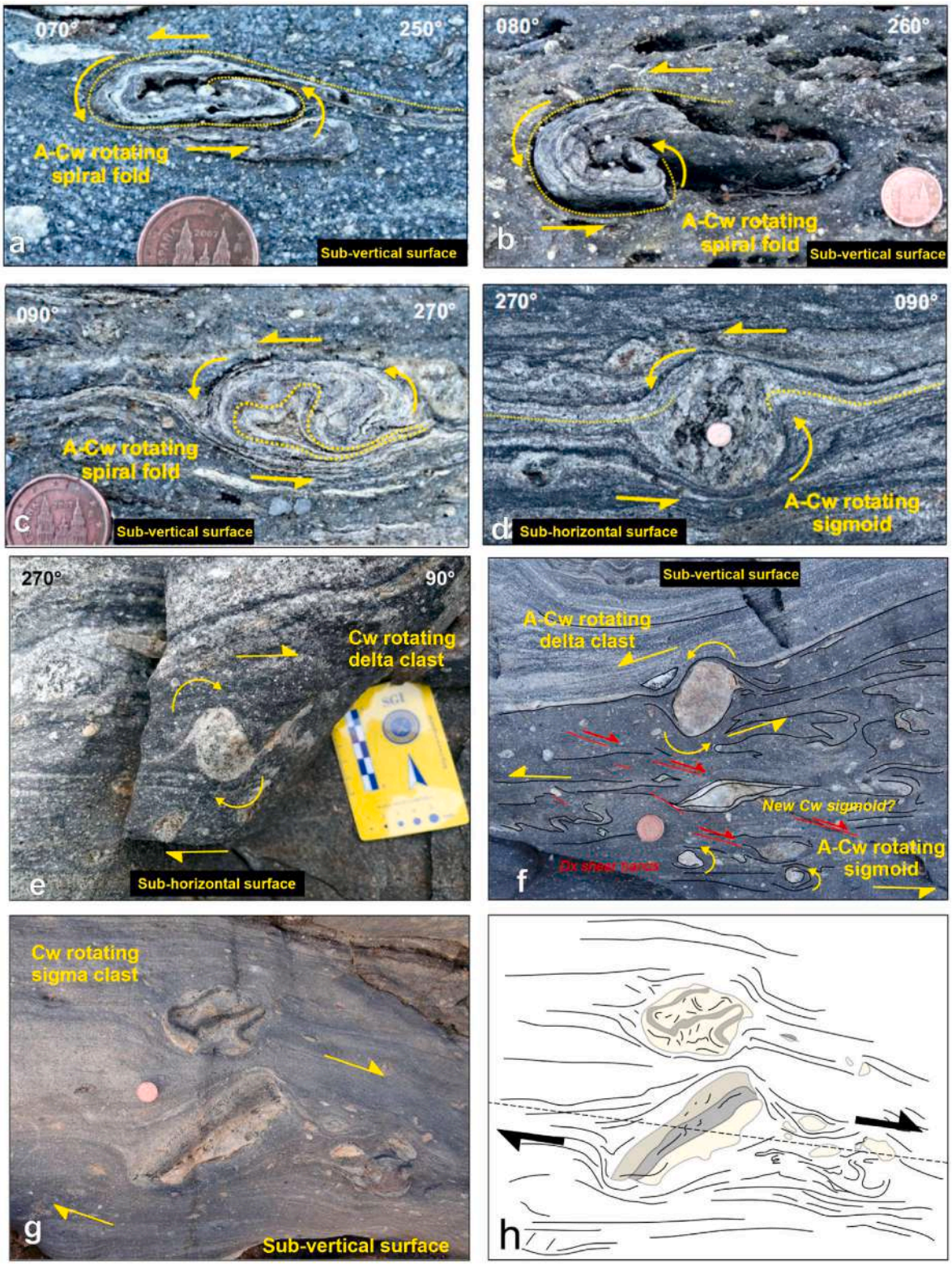

Fig. 16. a–c) rotating spiral folds associated with sinistral shear; d) sigmoidal clast at Site 3 (cf. Fig. 13f); e-f) δ - and σ- (sigma) type clasts showing variable shear sense; g) sigmoid dextral clast into fine grained mylonitic marbles; h) interpretation of picture shown in g).

fold (recognized at Site 2 – Fig. 11a), synthetic dextral shear bands, sigmoid clasts.

CRediT authorship contribution statement

E. Fazio: Writing – review & editing, Writing – original draft, Visualization, Validation, Supervision, Software, Resources, Project administration, Methodology, Investigation, Funding acquisition, Formal analysis, Data curation, Conceptualization. **G. Ortolano:** Writing – review & editing, Writing – original draft, Validation, Software, Methodology, Investigation, Formal analysis, Data curation. **G.I. Alsop:** Writing – review & editing, Writing – original draft,

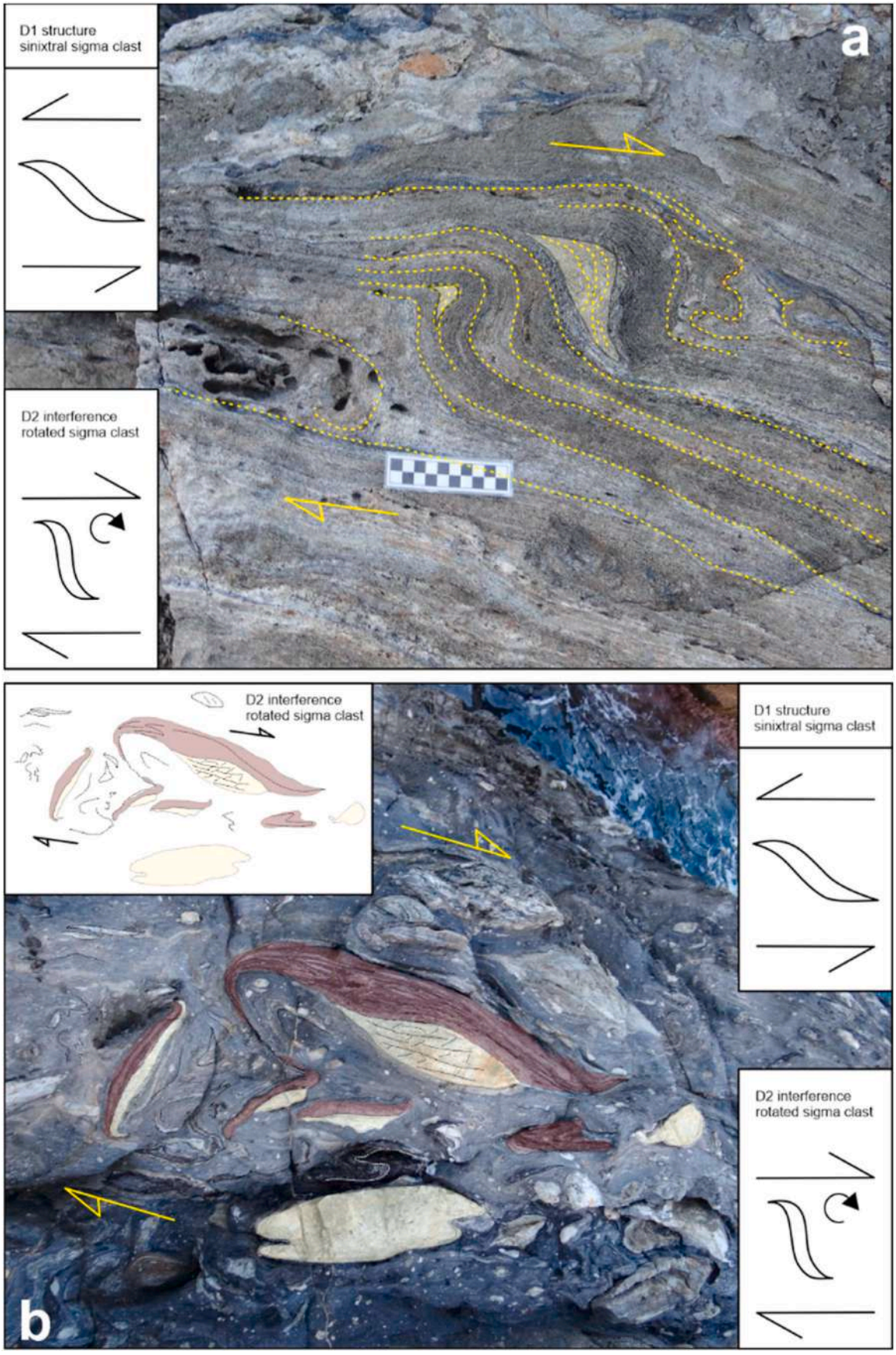

Fig. 17. a–b) Examples of interference patterns of rigid sigmoidal blocks affected by early sinistral shear and later overprinted by dextral shear.

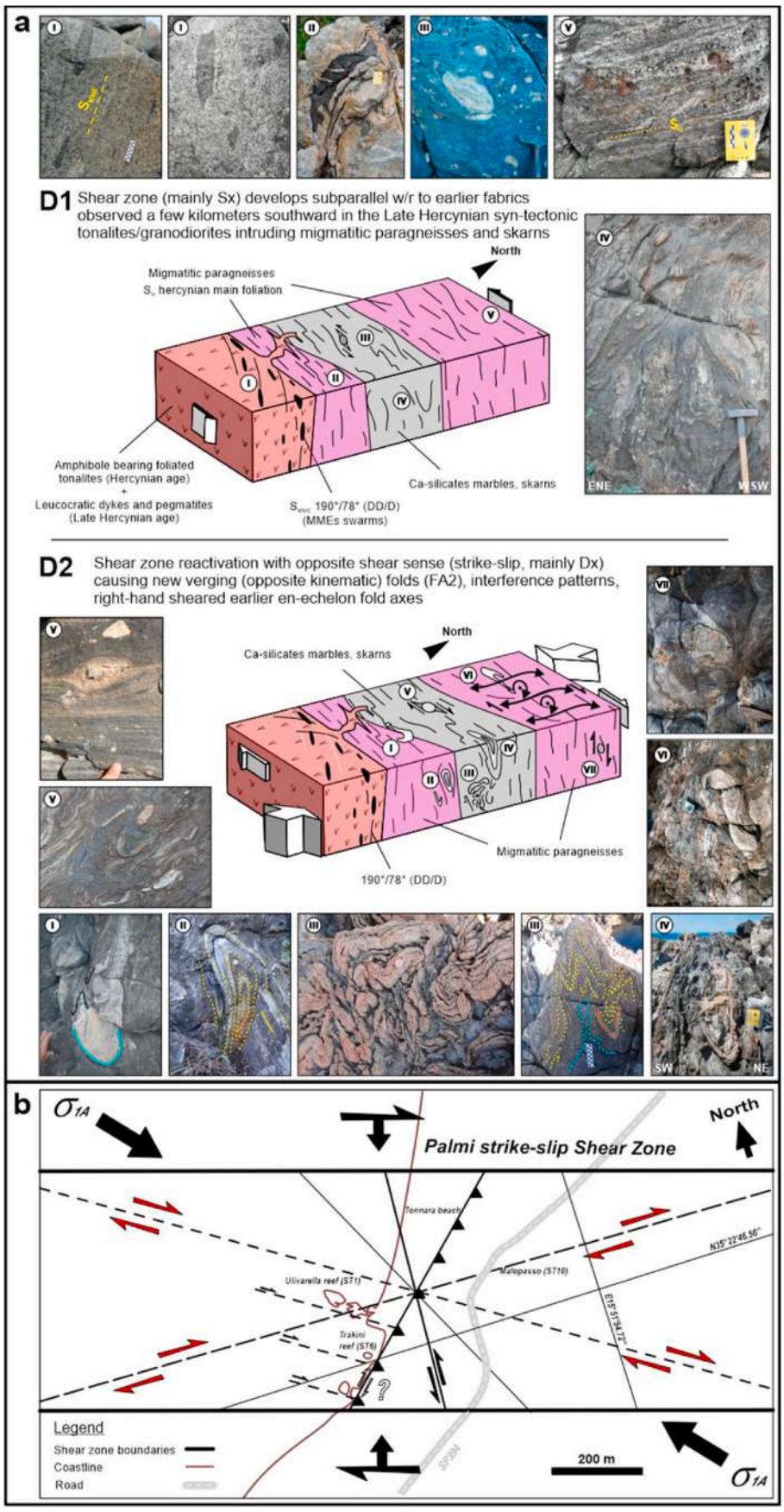

(caption on next page)

Fig. 18. a) 3D geological cartoon (not to scale) summarizing the evolution of the PSZ for the deformation phases D1 and D2, together with various typical mesoscopic structures (insets I-VII) recognized at various outcrop sites. The S_{MME} depicted in D1 (inset I) is the main trend of a plane defined by the major axes of sub-parallel microgranular mafic enclaves (mainly oblate ellipsoid in shape) found within late Hercynian tonalites outcropping in the Rovaglioso locality (Grande et al., 2009), a few kilometers south of the PSZ along the sea coastline (see Fig. 2b). The S_H foliation depicted in D1 (inset V) is the Hercynian foliation of garnet-bearing migmatites belonging to the so called Diorito-Kinzigitic Unit of Calabria (Novarese, 1931; Schenk, 1981) outcropping in the Taureana beach a few kilometers north of PSZ; b) Schematic geological map of the study area showing the orientation of the Alpine ductile-brittle low angle thrust exposed at Sites 7–8 (see Fig. 3), which is compatible with a general dextral shear sense along the strike-slip plane of the PSZ developed during the D3 tectonic phases (see Table 2).

Visualization, Validation, Supervision, Project administration, Methodology, Investigation, Formal analysis, Data curation, Conceptualization. **A. D'Agostino:** Writing – review & editing, Visualization, Validation, Software, Methodology, Investigation, Formal analysis, Data curation. **R. Visalli:** Writing – review & editing, Writing – original draft, Visualization, Validation, Software, Methodology, Investigation, Formal analysis. **V. Luzin:** Writing – original draft, Visualization, Validation, Supervision, Software, Resources, Methodology, Investigation, Funding acquisition, Formal analysis, Data curation, Conceptualization. **F. Salvemini:** Writing – original draft, Visualization, Validation, Software, Methodology, Investigation, Formal analysis, Data curation, Conceptualization. **R. Cirrincione:** Writing – review & editing, Validation, Supervision, Project administration, Funding acquisition, Formal analysis.

Data availability

Data will be made available on request.

Acknowledgements

Stefano Pannucci is deeply acknowledged for his support with UAV flights and field/aerial photo acquisition during the first survey campaign. Mario Pagano is thanked for a preliminary GIS dataset elaboration of structural elements. E.F. and V.L. acknowledge the use of ANSTO instrumentation (in this case diffractometer KOWARI) hosted at Sidney laboratory. E.F. expresses gratitude to Carmelo Fiorillo for his accommodation and hospitality and for the boat trip to Ulivarella Stacks. E.F. is grateful to Laboratorio Sezioni Sottili at the Department of Biol. Geol. Env. Sciences of Catania University for thin sections preparations. G.I.A. gratefully acknowledges support from the Erasmus Exchange Programme. This study has been financially supported by University of Catania (PIAno di inCEntivi per la RIcerca di Ateneo 2020/2022—Pia.Ce.Ri), Grant Number: 22722132153, within the project: "Combined geomatic and petromatic applications: The new frontier of geoscience investigations from field-to microscale (GeoPetroMat)".

Elena Druguet and an anonymous reviewer are deeply acknowledged for their constructive review that allowed us to clarify and improve the earlier version of the manuscript. We are grateful to Fabrizio Agosta for his efficient editorial handling and useful suggestions.

Appendix A. Supplementary data

Supplementary data to this article can be found online at https://doi.org/10.1016/j.jsg.2024.105213.

Additional Materials

Agisoft Cloud 3D VOM of a portion of the Site 1 (Ulivarella Reef) is available at the following weblink https://cloud.agisoft.com/shared/projects/1dccb506-0117-4045-ac48-ad633a58d100.

The Site 1 (entire outcrop) point cloud is available here: https://cloud.agisoft.com/shared/projects/cc156bcd-a1ce-4b7d-9add-9839b16f28ba.

Some point of interest for Site 2 (Orthomosaic) are available here: https://cloud.agisoft.com/shared/projects/020d3efa-474e-4769-a6be-f8851a61d9c0.

.KMZ files of 3D virtual outcrop models to be processed with Geovis3D software are available at: https://data.mendeley.com/datasets/f7z9ppz982/1.

References

Aerden, D.G.A.M., Ruiz-Fuentes, A., 2020. X-ray computed micro-tomography of spiral garnets: a new test of how they form. J. Struct. Geol. 136, 104054 https://doi.org/10.1016/j.jsg.2020.104054.

Aerden, D.G.A.M., Farrell, T.P., Baxter, E.F., Stewart, E.M., Ruiz-Fuentes, A., Bouybaouene, M., 2022. Refined tectonic evolu.on of the Be.c-Rif orogen through integrated 3-D microstructural analysis and Sm-Nd da.ng of garnet porphyroblasts. Tectonics 41, e2022TC007366. https://doi.org/10.1029/2022TC007366.

Alsop, G.I., 1992. Progressive deformation and the rotation of contemporary fold axes in the Ballybofey Nappe, northwest Ireland. Geol. J. 27, 271–283.

Alsop, G.I., Holdsworth, R.E., 1993. The distribution, geometry and kinematic significance of Caledonian buckle folds in the western Moine Nappe, northwest Scotland. Geol. Mag. 130, 353–362.

Alsop, G.I., 1994. Relationships between distributed and localised shear in the tectonic evolution of a Caledonian fold and thrust zone, northwest Ireland. Geol. Mag. 131, 123–136.

Alsop, G.I., Holdsworth, R.E., Strachan, R.A., 1996. The generation and geometry of transport-parallel cross folds within a mid-crustal Caledonian thrust stack, northern Scotland. J. Struct. Geol. 18, 783–790.

Alsop, G.I., Holdsworth, R.E., 2002. The geometry and kinematics of flow perturbation folds. Tectonophysics 350, 99–125. https://doi.org/10.1016/S0040-1951(02)00084-7.

Alsop, G.I., Holdsworth, R.E., 2004. Shear zone folds: records of flow perturbation or structural inheritance? Flow Processes in Faults and Shear Zones 224, 177–199.

Alsop, G.I., Carreras, J., 2007. The structural evolution of sheath folds: A case study from Cap de Creus. J. Struct. Geol. 29, 1915–1930. https://doi.org/10.1016/j.jsg.2007.09.010.

Alsop, G.I., Cheer, D.A., Strachan, R.A., Krabbendam, M., Kinny, P.D.E., Leslie, A.G., 2010. Progressive fold and fabric evolution associated with regional strain gradients: a case study from across a Scandian ductile thrust nappe, Scottish Caledonides. In: Law, R.D.,W.H., Holdsworth, R., Krabbendam, M., Strachan, R.A. (Eds.), Continental Tectonics and Mountain Building: the Legacy of Peach and Horne, vol. 335. Geological Society, London, Special Publications, pp. 253–272. https://doi.org/10.1144/SP335.12.

Alsop, G.I., Holdsworth, R.E., 2012. The three dimensional shape and localisation of deformation within multilayer sheath folds. J. Struct. Geol. 44, 110–128.

Alsop, G.I., Strachan, R.A., Holdsworth, R.E., Burns, I.M., 2021. Geometry of folded and boudinaged pegmatite veins emplaced within a strike-slip shear zone: a case study from the Caledonian orogen, northern Scotland. J. Struct. Geol. 142, 104233 https://doi.org/10.1016/j.jsg.2020.104233.

Angì, G., Cirrincione, R., Fazio, E., Fiannacca, P., Ortolano, G., Pezzino, A., 2010. Metamorphic evolution of preserved hercynian crustal section in the Serre massif (Calabria-Peloritani orogen, southern Italy). Lithos 115, 237–262. https://doi.org/10.1016/j.lithos.2009.12.008.

Arslan, A., Passchier, C.W., Koehn, D., 2008. Foliation boudinage. J. Struct. Geol. 30, 291–309. https://doi.org/10.1016/j.jsg.2007.11.004.

Bertolani, M., Loschi Ghittoni, A.G., 1977. Le rocce carbonate della formazione kinzigitica calabrese. Rendiconti della Soc. Ital. Mineral. Petrol. 33, 699–711.

Bond, C.E., Cawood, A.J., 2021. A role for virtual outcrop models in blended learning–improved 3D thinking and positive perceptions of learning. Geosci. Commun. 4, 233–244. https://doi.org/10.5194/gc-4-233-2021.

Cardozo, N., Allmendinger, R.W., 2013. Spherical projections with OSXStereonet. Comput. Geosci. 51 (0), 193–205. https://doi.org/10.1016/j.cageo.2012.07.021.

Carreras, J., Druguet, E., Griera, A., 2005. Shear zone-related folds. J. Struct. Geol. 27, 1229–1251. https://doi.org/10.1016/J.JSG.2004.08.004.

Carreras, J., Druguet, E., 2019. Complex fold patterns developed by progressive deformation. J. Struct. Geol. 125, 195–201. https://doi.org/10.1016/j.jsg.2018.07.015.

Cawood, A.J., Bond, C.E., Howell, J.A., Butler, R.W., Totake, Y., 2017. LiDAR, UAV or compass-clinometer? Accuracy, coverage and the effects on structural models. J. Struct. Geol. 98, 67–82. https://doi.org/10.1016/j.jsg.2017.04.004.

Cicolin, M.M., Bearman, P.W., Assi, G.R.S., Buxton, O.R.H., 2023. Bistability in the wake of a circular cylinder with passive control using two leeward rods. J. Fluid Struct. 120, 103918 https://doi.org/10.1016/j.jfluidstructs.2023.103918.

Cirrincione, R., Fazio, E., Fiannacca, P., Ortolano, G., Pezzino, A., Punturo, R., 2015. The Calabria-Peloritani Orogen, a composite terrane in Central Mediterranean; its overall architecture and geodynamic significance for a pre-Alpine scenario around the Tethyan basin. Period. Mineral. 84 (3B), 701–749. https://doi.org/10.2451/2015PM0446.

Cortese, E., 1885. Sull'esistenza di un dicco basaltico presso Palmi, in provincia di Reggio Calabria. Boll. R. Com. Geol. d'Italia 16, 11–12.

D'Agostino, A., 2023. New Frontiers of Mineralogical and Structural Data Analysis in the Era of Machine Learning: Tools for Modern Petrography [Doctoral Dissertation. University of Catania].
Dierick, M., Masschaele, B., Van Hoorebeke, L., 2004. Octopus, a fast and user-friendly tomographic reconstruction package developed in LabView. Meas. Sci. Technol. 15, 1366. https://doi.org/10.1088/0957-0233/15/7/020.
Dewey, J.F., Holdsworth, R.E., Strachan, R.A., 1998. Transpression and Transtension Zones, vol. 135. Geological Society, London, Special Publications, pp. 1–14. https://doi.org/10.1144/GSL.SP.1998.135.01.01.
Druguet, E., Alsop, G.I., Carreras, J., 2009. Coeval brittle and ductile structures associated with extreme deformation partitioning in a multilayer sequence. J. Struct. Geol. 31 (5), 498–511. https://doi.org/10.1016/j.jsg.2009.03.004.
Fazio, E., Cirrincione, R., Pezzino, A., 2008. Estimating P–T conditions of Alpine-type metamorphism using multistage garnet in the tectonic windows of the Cardeto area (southern Aspromonte Massif, Calabria). Mineral. Petrol. 93, 111–142. https://doi.org/10.1007/s00710-007-0216-2.
Fazio, E., Ortolano, G., Visalli, R., Alsop, I., Cirrincione, R., Pezzino, A., 2018. Strain localization and sheath fold development during progressive deformation in a ductile shear zone: a case study of macro-to micro-scale structures from the Aspromonte Massif, Calabria. Italian Journal of Geosciences. https://doi.org/10.3301/IJG.2018.09.
Fazio, E., 2019. Chapter 10 - recognition of structures in mid-crustal shear zones and how to discern between them. In: Billi, A., Fagereng, Å. (Eds.), Problems and Solutions in Structural Geology and Tectonics, Developments in Structural Geology and Tectonics. Elsevier, pp. 119–128. https://doi.org/10.1016/B978-0-12-814048-2.00010-7.
Fazio, E., Alsop, G.I., Nania, L., Graziani, R., Iaccarino, S., Montomoli, C., Carosi, R., Luzin, V., Salvemini, F., Gambino, S., Cirrincione, R., Mamtani, M.A., 2024. CPO and quantitative textural analyses within sheath folds. J. Struct. Geol. 178, 05000 https://doi.org/10.1016/j.jsg.2023.105000.
Festa, V., Prosser, G., Caggianelli, A., Grande, A., Langone, A., Mele, D., 2015. Vorticity analysis of the Palmi shear zone mylonites: new insights for the Alpine tectonic evolution of the Calabria–Peloritani terrane (southern Italy). Geol. J. 51, 670–681. https://doi.org/10.1002/gj.2673.
Festa, V., Cicala, M., Tursi, F., 2020. The Curinga–Girifalco Line in the framework of the tectonic evolution of the remnant Alpine chain in Calabria (southern Italy). Int. J. Earth Sci. 109, 2583–2598. https://doi.org/10.1007/s00531-020-01918-5.
Fiannacca, P., Williams, I.S., Cirrincione, R., 2017. Timescales and mechanisms of batholith construction: constraints from zircon oxygen isotopes and geochronology of the late Variscan Serre Batholith (Calabria, southern Italy). Lithos. https://doi.org/10.1016/j.lithos.2016.06.011.
Fiannacca, P., Russo, D., Fazio, E., Cirrincione, R., Mamtani, M.A., 2021. Fabric analysis in upper crustal post-collisional granitoids from the Serre batholith (Southern Italy): results from microstructural and ams investigations. Geosciences 11. https://doi.org/10.3390/geosciences11100414.
Finch, M.A., Bons, P.D., Weinberg, R.F., Llorens, M.G., Griera, A., Gomez-Rivas, E., 2022. A dynamic atlas of interference patterns in superimposed, opposite sense ductile shear zones. J. Struct. Geol. 165, 104739 https://doi.org/10.1016/j.jsg.2022.104739.
Forbes, C.J., Betts, P.G., Lister, G.S., 2004. Synchronous development of Type 2 and Type 3 fold interference patterns: evidence for recumbent sheath folds in the Allendale Area, Broken Hill, NSW, Australia. J. Struct. Geol. 26 (1), 113–126. https://doi.org/10.1016/S0191-8141(03)00074-9.
Fossen, H., Cavalcante, G.C.G., 2017. Shear zones – a review. Earth Sci. Rev. 171, 434–455. https://doi.org/10.1016/J.EARSCIREV.2017.05.002.
Fossen, H., Cavalcante, G.C.G., Pinheiro, R.V.L., Archanjo, C.J., 2019. Deformation–progressive or multiphase? J. Struct. Geol. 125, 82–99. https://doi.org/10.1016/j.jsg.2018.05.006.
Gardner, R., Piazolo, S., Evans, L., Daczko, N., 2017. Patterns of strain localization in heterogeneous, polycrystalline rocks – a numerical perspective. Earth Planet Sci. Lett. 463, 253–265. https://doi.org/10.1016/j.epsl.2017.01.039.
Gorbunov, I.A., Balagansky, V.V., 2022. Spiral-shaped fabrics in metamorphic rocks: a new example of rotation during progressive deformation. J. Struct. Geol. 159, 104590 https://doi.org/10.1016/j.jsg.2022.104590.
Grande, A., Vincenzo, G.D., Prosser, G., Caggianelli, A., 2009. Direct evidence of Middle Oligocene extension in the Calabria - Peloritani terrane from co-seismic faulting: the pseudotachylyte-bearing shear zones of Palmi (southern Calabria, Italy). Terra. Nova 21. https://doi.org/10.1111/j.1365-3121.2009.00884.x.
Grasemann, B., Stüwe, K., Vannay, J.-C., 2003. Sense and non-sense of shear in flanking structures. J. Struct. Geol. 25, 19–34. https://doi.org/10.1016/S0191-8141(02)00012-3.
Grasemann, B., Dabrowski, M., 2015. Winged inclusions: pinch-and-swell objects during high-strain simple shear. J. Struct. Geol. 70, 78–94. https://doi.org/10.1016/j.jsg.2014.10.017.
Griera, A., Llorens, M.-G., Gomez-Rivas, E., Bons, P.D., Jessell, M.W., Evans, L.A., Lebensohn, R., 2013. Numerical modelling of porphyroclast and porphyroblast rotation in anisotropic rocks. Tectonophysics 587, 4–29. https://doi.org/10.1016/j.tecto.2012.10.008.
Hippertt, J., Tohver, E., 2002. Interaction of flexural shear, S–C fabrics, and oblique shear during folding of micaceous quartzite. J. Struct. Geol. 24, 1087–1099. https://doi.org/10.1016/S0191-8141(01)00093-1.
Holdsworth, R.E., Stewart, M., Imber, J., Strachan, R.A., 2001. The Structure and Rheological Evolution of Reactivated Continental Fault Zones: A Review and Case Study. Geological Society Special Publication. https://doi.org/10.1144/GSL.SP.2001.184.01.07.
Holdsworth, R.E., Tavarnelli, E., Clegg, P., Pinheiro, R.V.L., Jones, R.R., McCaffrey, K.J.W., 2002. Domainal deformation patterns and strain partitioning during transpression: an example from the Southern Uplands terrane, Scotland. J. Geol. Soc. 159 (4), 401–415. https://doi.org/10.1144/0016-764901-123.
Iacopini, D., Carosi, R., Xypolias, P., 2010. Implications of complex eigenvalues in homogeneous flow: a three-dimensional kinematic analysis. J. Struct. Geol. 32, 93–106. https://doi.org/10.1016/j.jsg.2009.10.003.
Kirstein, O., Luzin, V., Garbe, U., 2009. The strain-scanning diffractometer kowari. Neutron News 20 (4), 34–36.
Lin, S., Jiang, D., Williams, P.F., 1998. Transpression (Or Transtension) Zones of Triclinic Symmetry: Natural Example and Theoretical Modelling, vol. 135. Geological Society Special Publication, pp. 41–57. https://doi.org/10.1144/GSL.SP.1998.135.01.04.
Ma, X., Tang, Z., Jiang, N., 2022. Investigation of spanwise coherent structures in turbulent backward-facing step flow by time-resolved PIV. Exp. Therm. Fluid Sci. 132, 110569 https://doi.org/10.1016/j.expthermflusci.2021.110569.
Mandal, N., Samanta, S.K., Chakraborty, C., 2001. Numerical modeling of heterogeneous flow fields around rigid objects with special reference to particle paths, strain shadows and foliation drag. Tectonophysics 330, 177–194. https://doi.org/10.1016/S0040-1951(00)00223-7.
Marques, F.O., Schmid, D.W., Andersen, T.B., 2007. Applications of inclusion behaviour models to a major shear zone system: the Nordfjord-Sogn Detachment Zone in western Norway. J. Struct. Geol. 29, 1622–1631. https://doi.org/10.1016/j.jsg.2007.05.008.
Marques, F.O., Burlini, L., 2008. Rigid inclusions rotate in geologic materials as shown by torsion experiments. J. Struct. Geol. 30, 1368–1371. https://doi.org/10.1016/j.jsg.2008.07.002.
Micheletti, F., Fornelli, A., Piccarreta, G., Barbey, P., Tiepolo, M., 2008. The basement of Calabria (southern Italy) within the context of the Southern European Variscides: LA-ICPMS and SIMS U–Pb zircon study. Lithos 104 (1–4), 1–11. https://doi.org/10.1080/00206814.2011.623022.
Mies, J.W., 1993. Structural-analysis of sheath folds in the sylacauga-marble-group, talladega salte belt, southern appalachians. J. Struct. Geol. 15 (8), 983–993.
Mukherjee, S., 2017. Review on symmetric structures in ductile shear zones. Int. J. Earth Sci. 106, 1453–1468. https://doi.org/10.1007/s00531-016-1366-4.
Ortolano, G., Cirrincione, R., Pezzino, A., 2005. PT evolution of alpine metamorphism in the southern Aspromonte massif (Calabria-Italy). Schweiz. Mineral. Petrogr. Mitt 85 (1), 31–56.
Ortolano, G., Cirrincione, R., Pezzino, A., Puliatti, G., 2013. Geo-Petro-Structural study of the Palmi shear zone: kinematic and rheological implications. Rend. Online Soc. Geol. Ital 29, 126–129.
Ortolano, G., Fazio, E., Visalli, R., Alsop, G.I., Pagano, M., Cirrincione, R., 2020. Quantitative microstructural analysis of mylonites formed during Alpine tectonics in the western Mediterranean realm. J. Struct. Geol. 131, 103956 https://doi.org/10.1016/j.jsg.2019.103956.
Ortolano, G., D'Agostino, A., Pagano, M., Visalli, R., Zucali, M., Fazio, E., Alsop, I., Cirrincione, R., 2021. ArcStereoNet: a new ArcGIS® toolbox for projection and analysis of meso-and micro-structural data. ISPRS Int. J. Geo-Inf. 10 (2), 50. https://doi.org/10.3390/ijgi10020050.
Passchier, C.W., 1998. Monoclinic model shear zones. J. Struct. Geol. 20, 1121–1137. https://doi.org/10.1016/S0191-8141(98)00046-7.
Piette-Lauzière, N., Larson, K.P., Kellett, D.A., Graziani, R., 2020. Intracrystalline vorticity record of flow kinematics during shear zone reactivation. J. Struct. Geol. 140, 104134 https://doi.org/10.1016/j.jsg.2020.104134.
Platt, J.P., 1983. Progressive refolding in ductile shear zones. J. Struct. Geol. 5 (6), 619–622.
Platt, J.P., Behr, W.M., 2011. Grainsize evolution in ductile shear zones: implications for strain localization and the strength of the lithosphere. J. Struct. Geol. 33 (4), 537–550. https://doi.org/10.1016/j.jsg.2011.01.018.
Prosser, G., Caggianelli, A., Rottura, A., Moro, A.D., 2003. Strain localisation driven by marble layers: the Palmi shear zone (Calabria-Peloritani terrane, Southern Italy). Geoacta 2.
Ramsay, J.G., 1980. Shear zone geometry: a review. J. Struct. Geol. 2, 83–99. https://doi.org/10.1016/0191-8141(80)90038-3.
Reddy, S.M., Wheeler, J., Butler, R.W.H., Cliff, R.A., Freeman, S., Inger, S., Pickles, C., Kelley, S.P., 2003. Kinematic reworking and exhumation within the convergent Alpine Orogen. Tectonophysics 365, 77–102. https://doi.org/10.1016/S0040-1951(03)00017-9.
Reddy, G.P.O., 2018. Digital Image Processing: Principles and Applications. Springer International Publishing, New York.
Russo, D., Fiannacca, P., Fazio, E., Cirrincione, R., Mamtani, M.A., 2023. From floor to roof of a batholith: geology and petrography of the north-eastern Serre Batholith (Calabria, southern Italy). J. Maps 19, 2149358. https://doi.org/10.1080/17445647.2022.2149358.
Schulmann, K., Edel, J.-B., Martínez Catalán, J.R., Mazur, S., Guy, A., Lardeaux, J.-M., Ayarza, P., Palomeras, I., 2022. Tectonic evolution and global crustal architecture of the European Variscan belt constrained by geophysical data. Earth Sci. Rev. 234, 104195 https://doi.org/10.1016/j.earscirev.2022.104195.
Smeraglia, L., Mercuri, M., Tavani, S., Pignalosa, A., Kettermann, M., Billi, A., Carminati, E., 2021. 3D Discrete Fracture Network (DFN) models of damage zone fluid corridors within a reservoir-scale normal fault in carbonates: multiscale approach using field data and UAV imagery. Mar. Petrol. Geol. 126, 104902 https://doi.org/10.1016/j.marpetgeo.2021.104902.
Tavani, S., Billi, A., Corradetti, A., Mercuri, M., Bosman, A., Cuffaro, M., Seers, T., Carminati, E., 2022. Smartphone assisted fieldwork: towards the digital transition of geoscience fieldwork using LiDAR-equipped iPhones. Earth Sci. Rev. 227, 103969 https://doi.org/10.1016/j.earscirev.2022.103969.

Tavarnelli, E., Holdsworth, R.E., Clegg, P., Jones, R.R., McCaffrey, K.J.W., 2004. The anatomy and evolution of a transpressional imbricate zone, Southern Uplands, Scotland. J. Struct. Geol. 26, 1341–1360. https://doi.org/10.1016/j.jsg.2004.01.003.

Thiele, S.T., Grose, L., Samsu, A., Micklethwaite, S., Vollgger, S.A., Cruden, A.R., 2017. Rapid, semi-automatic fracture and contact mapping for point clouds, images and geophysical data. Solid Earth 8, 1241–1253. https://doi.org/10.5194/se-8-1241-2017.

Tóth, Z., Lafrance, B., Dubé, B., 2023. Oblique lateral extrusion during dextral transpression along the Beardmore-Geraldton belt, Canada. J. Struct. Geol. 169, 104834 https://doi.org/10.1016/j.jsg.2023.104834.

Tripodi, V., Muto, F., Brutto, F., Perri, F., Critelli, S., 2018. Neogene-Quaternary evolution of the forearc and backarc regions between the Serre and Aspromonte Massifs, Calabria (southern Italy). Mar. Petrol. Geol. 95, 328–343. https://doi.org/10.1016/j.marpetgeo.2018.03.028.

van Hinsbergen, D.J.J., Torsvik, T.H., Schmid, S.M., Maţenco, L.C., Maffione, M., Vissers, R.L.M., Gürer, D., Spakman, W., 2020. Orogenic architecture of the Mediterranean region and kinematic reconstruction of its tectonic evolution since the Triassic. Gondwana Res. 81, 79–229. https://doi.org/10.1016/j.gr.2019.07.009.

Vasuki, Y., Holden, E.-J., Kovesi, P., Micklethwaite, S., 2014. Semi-automatic mapping of geological Structures using UAV-based photogrammetric data: an image analysis approach. Comput. Geosci. 69, 22–32. https://doi.org/10.1016/j.cageo.2014.04.012.

Visalli, R., Ortolano, G., Godard, G., Cirrincione, R., 2021. Micro-fabric analyzer (mfa): a new semiautomated ArcGIS-based edge detector for quantitative microstructural analysis of rock thin-sections. ISPRS Int. J. Geo-Inf. 10, 51. https://doi.org/10.3390/ijgi10020051.

Vitale, S., Mazzoli, S., 2008. Heterogeneous shear zone evolution: the role of shear strain hardening/softening. J. Struct. Geol. 30, 1383–1395. https://doi.org/10.1016/j.jsg.2008.07.006.

Vitale, S., Ciarcia, S., Fedele, L., Tramparulo, F.D., 2019. The Ligurian oceanic successions in southern Italy: the key to decrypting the first orogenic stages of the southern Apennines-Calabria chain system. Tectonophysics 750, 243–261. https://doi.org/10.1016/j.tecto.2018.11.010.

von Raumer, J.F., Stampfli, G.M., Bussy, F., 2003. Gondwana-derived microcontinents — the constituents of the Variscan and Alpine collisional orogens. Tectonophysics 365, 7–22. https://doi.org/10.1016/S0040-1951(03)00015-5.

von Raumer, J.F., Bussy, F., Schaltegger, U., Schulz, B., Stampfli, G.M., 2013. Pre-mesozoic alpine basements-their place in the European paleozoic framework. Bull. Geol. Soc. Am. 125, 89–108. https://doi.org/10.1130/B30654.1.

Weisstein, E.W., 2013. Ellipsoid. From Math World A Wolfram Web Resource. https://mathworld.wolfram.com/Ellipsoid.html.

Xypolias, P., 2010. Vorticity analysis in shear zones: a review of methods and applications. J. Struct. Geol. 32, 2072–2092. https://doi.org/10.1016/j.jsg.2010.08.009.

Xypolias, P., Alsop, G.I., 2014. Regional flow perturbation folding within an exhumation channel: a case study from the Cycladic Blueschists. J. Struct. Geol. 62, 141–155. https://doi.org/10.1016/j.jsg.2014.02.001.